

1 | **Linking glacially modified waters to catchment-scale subglacial discharge using
2 | autonomous underwater vehicle observations**

3 |
4 | L. A. Stevens¹, F. Straneo², S. B. Das³, A. J. Plueddemann², A. L. Kukulya⁴, and M. Morlighem⁵

5 |
6 | ¹Massachusetts Institute of Technology/Woods Hole Oceanographic Institution Joint Program in
Oceanography/Applied Ocean Science and Engineering, Woods Hole, MA 02543, USA

7 |
8 | ²Department of Physical Oceanography, Woods Hole Oceanographic Institution, Woods Hole,
MA 02543, USA

9 |
10 | ³Department of Geology and Geophysics, Woods Hole Oceanographic Institution, Woods Hole,
MA 02543, USA

11 |
12 | ⁴Department of Applied Ocean Physics and Engineering, Woods Hole Oceanographic Institution,
Woods Hole, MA 02543, USA

13 |
14 | ⁵Department of Earth System Science, University of California, Irvine, Croul Hall, Irvine, CA
92697, USA

15 | Correspondence to: L. A. Stevens (stevensl@mit.edu)

LAS 1/27/16 4:50 PM

Deleted: to subsurface glacially modified
waters near the front of a marine
terminating outlet glacier

LAS 1/27/16 4:50 PM

Deleted: an

20 **Abstract**

21 Measurements of near-ice (<200 meters) hydrography and near terminus subglacial hydrology
22 are lacking due in large part to the difficulty in working at the margin of calving glaciers. Here
23 we pair detailed hydrographic and bathymetric measurements collected with an Autonomous
24 Underwater Vehicle as close as 150 meters from the ice/ocean interface of the Sarqardliup
25 sermia/Sarqardleq Fjord system, West Greenland, with modeled and observed subglacial
26 discharge locations and magnitudes. We find evidence of two main types of subsurface glacially
27 modified water (GMW) with distinct properties and locations. The two GMW locations also
28 align with modeled runoff discharged at separate locations along the grounded margin
29 corresponding with two prominent subcatchments beneath Sarqardliup sermia. Thus, near-ice
30 observations and subglacial discharge routing indicate that runoff from this glacier occurs
31 primarily at two discrete locations and gives rise to two distinct glacially modified waters.
32 Furthermore, we show that the location with the largest subglacial discharge is associated with
33 the lighter, fresher glacially modified watermass. This is qualitatively consistent with results
34 from an idealized plume model.

35

36 **1. Introduction**

37 Greenland Ice Sheet mass loss quadrupled over the last two decades, contributing roughly
38 7.4 mm to global sea level rise from 1992-2011 (Shepherd et al., 2012), and increasing
39 freshwater inputs into the North Atlantic (Bamber et al., 2012). Ice sheet mass loss occurs
40 through runoff of surface melt, ice discharge through iceberg calving, and submarine melt at
41 marine-terminating outlet glacier margins (van den Broeke et al., 2009; Enderlin et al., 2014).
42 The synchronous retreat and speedup of marine-terminating glaciers in southeast Greenland in

LAS 1/27/16 4:50 PM
Deleted: localized in space and
LAS 1/27/16 4:50 PM
Deleted: that are consistent
LAS 1/27/16 4:50 PM
Deleted: two
LAS 1/27/16 4:50 PM
Deleted: . These locations, in turn, correspond
LAS 1/27/16 4:50 PM
Deleted: subglacial
LAS 1/27/16 4:50 PM
Deleted: subglacial discharge
LAS 1/27/16 4:50 PM
Deleted: only
LAS 1/27/16 4:50 PM
Deleted: primary
LAS 1/27/16 4:50 PM
Deleted: flux

53 the early 2000s was likely initiated by a dynamic change at marine termini (van den Broeke et
54 al., 2009; Rignot and Kanagaratnam, 2006; Thomas et al., 2009), and points towards common
55 external forcings from the warming atmosphere (Box et al., 2009) and/or ocean around
56 Greenland (Straneo and Heimbach, 2013), though the exact forcing mechanisms and relative
57 magnitudes remain unclear (Joughin et al., 2012; Straneo et al., 2013).

58 Increased submarine melt rates at outlet glacier marine termini may be a leading cause of
59 Greenland Ice Sheet outlet glacier speed up and retreat (Holland et al., 2008; Joughin et al.,
60 2012; Modyka et al., 2013; Post et al., 2011). The heat to drive submarine melting is supplied by
61 waters from the subpolar North Atlantic and Arctic seas, whose circulation inside the fjords is a
62 result of processes across a range of spatiotemporal scales (Jackson et al., 2014; Straneo et al.,
63 2010). Ultimately, melt rates are affected by ocean properties (temperature and stratification) and
64 circulation in near-ice waters (<200 m) (Jenkins et al., 2010). Submarine melting is thought to be
65 enhanced in summer as a result of meltwater runoff along the ice sheet bed entering the fjord
66 across the grounding line as subglacial discharge, which provides an additional buoyancy source
67 alongside submarine melt for initiating buoyant plumes along the terminus face (Jenkins, 1999,
68 2011; Sciascia et al., 2013; Xu et al., 2013). Relatively fresh waters rising in the core of these
69 plumes become denser as they entrain salty ambient fjord waters, and this entrainment driven by
70 plumes serves as a mechanism for transporting ambient fjord waters to the glacier face (Jenkins,
71 1999, 2011; Sciascia et al., 2013; Xu et al., 2013).

72 Plume theory and models combined with melt rate parameterizations suggest that higher
73 subglacial discharge rates are associated with faster flows and entrainment of a greater volume of
74 ambient fjord waters leading to higher submarine melt rates (Jenkins, 1999, 2011; Sciascia et al.,
75 2013; Xu et al., 2013; Carroll et al., 2015), however ocean property and plume measurements

LAS 1/27/16 4:50 PM

Deleted: of

LAS 1/27/16 4:50 PM

Deleted: Seas

LAS 1/27/16 4:50 PM

Deleted: serve

LAS 1/27/16 4:50 PM

Deleted: drive higher

LAS 1/27/16 4:50 PM

Deleted: and

needed to inform and validate model simulations and theory are lacking due to difficulty in working at the margin of calving glaciers (Straneo and Cenedese, 2015). As a result, current modeling-sourced estimates of submarine melt rates at tidewater glaciers and their sensitivity to external forcings of the near-ice environment are highly uncertain, and based on unconstrained models of plume dynamics using ice/ocean boundary parameterizations forced by far field (>1 km) ocean property measurements and largely unknown subglacial discharge magnitude and distribution (Jenkins, 2011; Kimura et al., 2014; Sciascia et al., 2013; Slater et al., 2015; Xu et al., 2012, 2013). For example, in a recent numerical study the spatial distribution of subglacial discharge along the grounding line was found to have a large effect on both the total submarine melt rate and its distribution along marine termini (Slater et al., 2015). With a lack of observations of both the near-ice environment and subglacial discharge configurations, we are unable to define likely subglacial discharge scenarios and their associated influence on ice/ocean interactions, resulting in an inadequate and untested understanding of how tidewater glaciers respond to oceanic forcing now and in the future (Straneo and Cenedese, 2015). Specifically, ocean measurements collected at distances >1 km from the glacier terminus provide limited information on the near-ice processes because the signals of glacial modification have, by that time, largely been smeared by lateral mixing processes. Indeed, the picture that emerges from such far-field measurements is of a horizontally invariant overturning cell(s) (Chauché et al., 2014; Inall et al., 2014; Johnson et al., 2011; Mortensen et al., 2011; Straneo et al., 2011; Sutherland et al., 2014).

In this study, we present fjord hydrography and bathymetry measurements from the near-ice environment of a tidewater glacier in west Greenland (Fig. 1) that allow us to reconstruct the distribution of subglacial discharge and provide key details on the ice-ocean exchanges. We do

LAS 1/27/16 4:50 PM

Deleted: fluxes

105 this by identifying the distribution of Glacially Modified Waters (GMW)—a product of ambient
106 | fjord waters mixing with subglacial discharge and glacial melt, including cooling due the melting
107 | of ice (Jenkins, 2011; Straneo et al., 2011)—within a few 100 m of the glacier face, and by
108 delineating the subglacial catchments that route subglacial meltwater to discharge locations
109 along the grounded terminus. These hydrographic measurements were obtained primarily in July
110 2012, using a REMUS-100 (Remote Environmental Measuring UnitS) Autonomous Underwater
111 Vehicle (AUV) (Fig. 2 a) to observe the temperature, salinity, and turbidity of waters in
112 Sarqardleq Fjord (SF) from ~2 km away to within a couple hundred meters of Sarqardliup sermia
113 (SS), a medium-sized tidewater glacier in West Greenland (68.90° N 50.32° W) (Fig. 1). This
114 novel, high-risk field campaign was successful in obtaining multiple vertical sections of fjord
115 water properties as close as 150 ± 25 m from the terminus as well as detailed bathymetry of the
116 previously unmapped fjord.

117

118 2. Field Campaign

119

120 2.1. REMUS-100 AUV

121 The REMUS-100 AUV is a small (1.8-m long) and light (45 kilograms) vehicle, rated to
122 100-m-depth that has been modified for under-ice exploration (Plueddemann et al., 2012) (Fig. 2
123 a). REMUS environmental sensors included a Neil Brown Ocean Systems conductivity-depth-
124 temperature (CTD) sensor, a WetLabs Environmental Characterization Optics (ECO) Triplet
125 | sensor, and a Teledyne/RDI dual upward and downward looking 1200 kHz Acoustic Doppler
126 | Current Profiler (ADCP). The ECO Triplet provides measurements of turbidity from backscatter
127 | at 660 nm. At the surface, REMUS communications include Iridium satellite telemetry,

LAS 1/27/16 4:50 PM

Deleted: Only measurements from the CTD and ECO Triplet are presented here.

130 FreeWave 900 MHz radio acoustic data telemetry, WiFi for local area network for wireless
131 testing and configuration, and a Global Positioning System (GPS) receiver for location fixes at
132 the start and end of missions. At depth, REMUS navigates by acoustically ranging to a network
133 of three moored Low Frequency (LF 10 kHz) Long BaseLine (LBL) transponders (Fig. 3). The
134 vehicle continuously updates its position while underway through a combination of dead
135 reckoning algorithms (which incorporate compass data, as well as propeller turns, water velocity
136 and bottom track data from the ADCP), LBL fixes, and surface GPS fixes when available (see
137 Plueddemann et al. 2012).

138 Field operations from the shore and in small boats took place from 17–27 July 2012
139 (DOY 199–209). SF is largely free of icebergs after spring sea ice break up, though frequent
140 calving along the SS terminus prevents boat travel within ~200 m of the terminus. REMUS
141 experienced navigational challenges in fjord environment due to a confluence of factors
142 including a strong surface pycnocline, loud and variable noise from calving and overturning of
143 icebergs, and heavy ice conditions preventing some GPS fixes. Transects presented here include
144 occasional deviations on the order of 5 to 50 m perpendicular to mission tracks. Data collected
145 during mission track deviations are accepted and collapsed back onto the transect line.

146 Deployed over the side of a small fishing boat, and eventually from the shore, 11
147 REMUS missions were completed over 9 days for both engineering and science objectives.

148 Although a minor issue for the localization of water properties, the navigation challenges and
149 track-line deviations caused significant uncertainties in the conversion from vehicle-relative to
150 earth-referenced velocities. As a result, only measurements from the CTD and ECO Triplet are
151 presented here. Combinations of yo-yo, fixed-depth, and fixed-altitude above bottom sampling
152 paths along transects parallel to the glacier face were used to acquire vertical sections of SF

LAS 1/27/16 4:50 PM

Deleted: Two Low Frequency (LF 10 kHz) LBL transponders were deployed in the fjord for AUV navigation (Fig. 3).

LAS 1/27/16 4:50 PM

Deleted: the iceberg-laden

157 water properties. In total, 5 transects of temperature, salinity, and turbidity along 5 terminus-
158 parallel sections (R1–R5 (Fig. 3)) at distances 150 to 1500 ± 25 m from the terminus selected
159 based on REMUS navigation quality and best across- and along-fjord coverage are presented in
160 this paper (Table 1).

161

162 2.2. Hydrographic and turbidity data

163 Profiles and sections presented here are made from along-track edited and smoothed
164 REMUS CTD and ECO data. REMUS temperature and salinity data were edited with the
165 removal of occasional erroneous points identified by an along-track first difference filter of
166 density calculated from the temperature and salinity measurements. First differences of >0.1
167 sigma were removed, affecting 0.2% of the data. Turbidity values were capped at 10
168 Nephelometric Turbidity Units (NTU). Raw temperature and salinity data were obtained at 0.22
169 s intervals, while turbidity measurements were taken at 1.15 s intervals. Temperature, salinity,
170 and turbidity measurements were interpolated to 0.5 s and then averaged over 2 s to obtain
171 smoothed, along-track data for all sensors on a common timebase with along-track resolution of
172 3.2–3.6 m (based on typical vehicle speeds that ranged between 1.6–1.8 m s⁻¹). Contour maps of
173 observed variables versus depth and distance were created from the REMUS mission tracks by
174 optimal interpolation (kriging) of measurements collapsed along glacier face-parallel transect
175 lines (Fig. 4). Simple, linear fits to computed autocorrelation were used for temperature, salinity,
176 and turbidity. Kriging was completed over a depth and along-track distance range slightly larger
177 than the data range, with a vertical resolution of 2 m and a horizontal resolution of 100 m, based
178 on the along-track resolution of 3 m and the horizontal distance between REMUS mid-depth

LAS 1/27/16 4:50 PM

Deleted: ~

LAS 1/27/16 4:50 PM

Deleted: for

LAS 1/27/16 4:50 PM

Deleted: of

LAS 1/27/16 4:50 PM

Deleted: .

183 sample lines of 100 m, respectively. Sensitivity tests of different kriging models and linear slopes
184 yielded little impact on resulting sections, demonstrating a robust kriging methodology.

185 Several shipboard CTD casts, collected using an RBR XR 620 CTD during the field
186 campaign, are presented to supplement the REMUS observations (Fig. 6). Eight shipboard CTD
187 casts were taken along the R1 transect (Fig. 3), 8 casts were taken along cross-fjord sections in
188 the outer SF (>10 km from the SS terminus) (triangles in Fig. 7 a), and 3 casts were taken
189 roughly at the R5 midpoint, northeastern end, and southwestern end (Fig. 3). REMUS and CTD
190 measurements were cross-calibrated by comparing REMUS R1 measurements with the 8 CTD
191 casts taken along the R1 transect immediately following the completion of the REMUS R1
192 mission. θ , S, and depth offsets were found to be 0.0015 °C, -0.05 PSU, and -2.5 m respectively,
193 between the CTD and REMUS measurements. The RBR XR 620 CTD was calibrated before and
194 after the fieldwork, but the REMUS CTD was not. REMUS measurements were therefore
195 adjusted by 2.5 m to match the CTD observations, and this offset is assumed to have remained
196 constant throughout the campaign.

197

198 **2.3. Bathymetric Data**

199 Detailed bathymetry of the previously unmapped SF was obtained through depth
200 measurements from a shipboard single-beam depth sounder, a shipboard ADCP, and the REMUS
201 downward looking ADCP in bottom-track mode (Fig. 3). After removing occasional spikes in
202 the REMUS ADCP depth soundings (outliers on order 15 m deeper than background), depth
203 measurements across the sampling platforms at crossover points were consistent within <4 m.
204 Coastline positions were assigned a depth of 0 m, and were obtained from digitizing a June 19,
205 2012 Landsat image (30-m horizontal resolution). Depth measurements were combined across

LAS 1/27/16 4:50 PM

Deleted: and

LAS 1/27/16 4:50 PM

Deleted: , taken

LAS 1/27/16 4:50 PM

Deleted: observations

LAS 1/27/16 4:50 PM

Deleted: 8

LAS 1/27/16 4:50 PM

Deleted: CTD

LAS 1/27/16 4:50 PM

Deleted: CTD

LAS 1/27/16 4:50 PM

Deleted: REMUS measurements were adjusted to match the CTD observations.

LAS 1/27/16 4:50 PM

Deleted: the SF coastline from

LAS 1/27/16 4:50 PM

Deleted: of the fjord were assigned a depth of 0 m and added to the dataset.

217 platforms by calculating a binned average depth measurement over a 25 x 25-m grid across the
218 fjord. The Barnes Objective Analysis (Barnes, 1994) was used to interpolate the binned depth
219 measurements with a 175 x 175-m search radius to create the bathymetry shown in Figure 3. The
220 bathymetry product aligns well with the binned depth measurements (less than 1 m offsets)
221 except in the location of the northern side of the seamount (68.92° N 50.34° W), which contains
222 the maximum offset from the gridded depth measurements at ± 5 m. Due to low data coverage,
223 the Barnes Objective Analysis was not extended to the outer regions of SF. However, with depth
224 measurements from the shipboard echosounder we have mapped the fjord centerline depth to the
225 confluence of SF and Tasiussaq Fjord, 15-km from the SS terminus (Figs. 1, 7 a).

226

227 **3. Physical Setting: The Sarqardleq Fjord/Sarqardliup sermia outlet glacier system**

228

229 **3.1. Fjord bathymetry, subglacial topography, and historical terminus positions**

230 The Sarqardliup sermia/Sarqardleq Fjord (SS/SF) outlet glacier/fjord system is located in
231 West Greenland roughly 30 km south of Jakobshavn Isbræ (Fig. 1). SS is a marine terminating
232 outlet glacier with a 6-km wide terminus and an upstream subglacial catchment area of 400 ± 50
233 km^2 (Fig. 7a, Table 3; methods described in section 3.2). We estimate total annual runoff out of
234 this catchment to be on the order of $1 \text{ km}^3 \text{ yr}^{-1}$ using Regional Atmospheric Climate Model
235 version 2.3 (RACMO2.3) runoff values (van den Broeke et al., 2009) (methods described in
236 section 3.2). A bedrock trough 100–150 m below sea level extends 15 km inland from the
237 terminus, and continues further inland as a bedrock trough above sea level (Morlighem et al.,
238 2014) (Fig. 7 a). The SS centerline ice thickness is ~ 200 m at the terminus and increases inland
239 (Morlighem et al., 2014) (Fig. 7 a). The Sarqardliup sermia terminus position has been relatively

LAS 1/27/16 4:50 PM

Deleted: 3.1. Sarqardleq Fjord
Bathymetry

LAS 1/27/16 4:50 PM

Deleted: Using RACMO2.3 runoff values
(van den Broeke et al., 2009) we

244 stable in comparison to the large terminus retreats observed at other Greenland tidewater glaciers
245 (Moon and Joughin, 2008) based on our analyses of LANDSAT imagery from 1979 to present
246 (Fig. 2 b). Modest advance and retreat phases on the order of ± 500 m are observed over recent
247 decades, with a net retreat of ~ 1 km within the center third of the glacier terminus observed from
248 1992 to present (Fig. 2 b). Average flow velocities within the SS outlet glacier during the 2007–
249 2009 winters were on order $125\text{--}175 \text{ m yr}^{-1}$, with the center third of the SS terminus reaching
250 speeds of 200 m yr^{-1} (Joughin et al., 2013).

251 The Sarqardleq-Tasiussaq fjord system is the southern side fjord off the larger, deeper
252 Jakobshavn Isbræ (JI) fjord, which connects the largest and fastest Greenland ice stream (JI) to
253 Disko Bugt (Fig. 1a). From the SS terminus, the shallower Sarqardleq-Tasiussaq Fjord system
254 extends roughly 30 km to the northwest before reaching JI fjord. SF meets Tasiussaq Fjord over
255 a previously unknown 70-m-deep sill, 15 km from the SS terminus (Figs. 1 & 7 a). Tasiussaq
256 Fjord meets JI fjord over an at most 125-m-deep sill (Gladish et al., 2015a) 30 km from the SS
257 terminus (Fig. 1). Waters along the SS terminus range from 20–150-m-depth, and are deepest in
258 two troughs near the center of the glacier (Fig. 2, Table 3). Both SS lateral terminus regions are
259 grounded in relatively shallow lagoons (<20 m) (Fig. 3). A 40-m-deep seamount is located 2.5
260 km from the vertical SS calving face (Fig. 3).

261

262 3.2. Subglacial catchment and runoff

263 To first order, subglacial catchments are defined by ice sheet surface and bed topography,
264 which governs subglacial hydraulic potential at the bed (Cuffey and Patterson, 2010). Gradients
265 in subglacial hydraulic potential at the ice-sheet bed do not completely dictate subglacial
266 meltwater pathways due to the constantly evolving subglacial hydraulic system over the summer

LAS 1/27/16 4:50 PM

Deleted: delineated

LAS 1/27/16 4:50 PM

Deleted: It is well known that gradients

269 melt season (Andrews et al., 2014; Chandler et al., 2013; Hewitt et al., 2012; Schoof, 2010), but
270 subglacial hydraulic potential gradients are likely the dominant regional factor. This is supported
271 by recent modeling studies, which find a strong topographic control of channelized subglacial
272 meltwater routing over Greenland Ice Sheet outlet glaciers (Banwell et al., 2013; Palmer et al.,
273 2011).

274 The SS catchment area was determined based on streamline analysis through subglacial
275 hydraulic potential gradient fields to estimate which path water parcels located at the bed under
276 inland ice will follow out to the coast. The downslope subglacial hydraulic potential gradient, $-\nabla\Phi_h$,
277 was calculated following:

278
$$-\nabla\Phi_h = -\rho_i g [f_w \nabla S + [\rho_w/\rho_i - f_w] \nabla B] \quad \text{eq. 1}$$

279 where ρ_i is the density of ice, ρ_w is the density of freshwater, g is the gravitational acceleration,
280 f_w is the flotation fraction, and ∇S and ∇B are the surface and bed gradients, respectively (Cuffey
281 and Patterson, 2010; Shreve, 1972). We assume water at the bed flows along the steepest
282 subglacial hydraulic potential gradient (Shreve, 1972). We used two widely available bedrock
283 elevation maps, Bamber et al. (2013) and Morlighem et al. (2014) (hereafter BBM2013 and
284 MBM2014) to calculate $-\nabla\Phi_h$ across a 1-km by 1-km grid (Bamber et al. 2013) and 150-m by
285 150-m grid (Morlighem et al. 2014) equivalent to the resolution of each bedrock elevation map.
286 MBM2014 beneath SS was updated from the previously published map, by adding our SF
287 bathymetry measurements as a boundary constraint along the SS terminus in this otherwise data-
288 sparse region. The MBM2014 used in this study is available online as IceBridge BedMachine
289 Greenland, Version 2 from the National Snow and Ice Data Center
290 (<http://nsidc.org/data/docs/daac/icebridge/idbmg4/index.html>). Surface ice gradients (∇S) are
291 calculated from the Greenland Ice Mapping Project (GIMP) Digital Elevation Model (Howat et

LAS 1/27/16 4:50 PM

Deleted: of supra- and subglacial meltwater routing

LAS 1/27/16 4:50 PM

Deleted: channeling of surface routing and

LAS 1/27/16 4:50 PM

Deleted: drainage systems occurs due to surface and bed gradients in both alpine valley glacier (Werder et al., 2013) and

LAS 1/27/16 4:50 PM

Deleted:) systems. Here we use a simple approach for calculating subglacial meltwater routing involving subglacial hydraulic potential gradients from two recent Greenland bedmaps (Bamber et al. 2013; Morlighem et al. 2014) and runoff values from the Regional Atmospheric Climate Model version 2.3 (RACMO2.3) (van den Broeke et al., 2009) over the calculated basal catchment area to estimate basal catchment boundaries (Fig. 7 a, Table 4) and the magnitude of subglacial runoff into SF (Fig. 7 b, Table 4)

LAS 1/27/16 4:50 PM

Deleted: bedrock elevation bedmaps

LAS 1/27/16 4:50 PM

Deleted: were used

LAS 1/27/16 4:50 PM

Deleted: bedmap. The

LAS 1/27/16 4:50 PM

Deleted: used

LAS 1/27/16 4:50 PM

Deleted: further

LAS 1/27/16 4:50 PM

Deleted: , with the addition of

316 al., 2014). The flotation fraction was set to $f_w = 1$ (basal water pressures are equal to ice
317 overburden pressure), which resulted in the maximum catchment area possible based on basal
318 hydraulic gradients in this region.

319 Surface runoff in the SS catchment for 2012 was determined from bilinear interpolation
320 of the 11-km grid resolution RACMO2.3 runoff values (3 grid cells within SS catchment) (van
321 den Broeke et al., 2009) to the 1-km grid from BMB2013 and the 150-m grid from MBM2014
322 (Fig. 7 a). Portions of the catchment lower than 400 m.a.s.l. were prescribed the same runoff
323 values as the RACMO2.3 grid point within the catchment at 432 m a.s.l. (68.82° N 50.19° W)
324 (Fig. 7 a), as there are no RACMO2.3 grid points at lower elevations within the catchment. We
325 assume that the ice-sheet bed is impermeable (does not store water) over the timescales
326 considered here, and that all surface runoff is transferred immediately to the bed directly beneath
327 the location of runoff formation at the ice sheet surface.

328

329 **4. Results**

330

331 **4.1 Glacially Modified Water (GMW) temperature, salinity, and turbidity properties in** 332 **Sarqardleq Fjord**

333 The summer Sarqardleq fjord waters are characterized by a ~10–20-m fresh and
334 relatively warm surface layer overlying a thick layer of weakly stratified, relatively salty
335 (S=30.5–32.5) and cold ($\theta \approx 1$ °C) waters (Table 2, Fig. 5 a, b). The summer fjord waters are the
336 same as the Surface Waters (SW) and Ilulissat Icefjord Waters (IIW) observed by recent
337 hydrographic surveys throughout Ilulissat Icefjord (Gladish et al., 2015a, 2015b). SW are a
338 mixture of IIW and fresher, warmer waters originating from local freshwater sources and

LAS 1/27/16 4:50 PM

Deleted: We find the

340 warmed by summer atmospheric forcing. IIW originates from Arctic Waters observed in Disko
341 and Baffin Bays (Gladish et al., 2015b) that enter SF after crossing sills at the mouth of JI fjord
342 (Schumann et al., 2012), the confluence of JI fjord and Tasiussaq fjord (Gladish et al., 2015a),
343 and the mouth of SF (Fig. 1). These summer fjord waters are observed in the outer SF by a set of
344 far-field CTD profiles taken near the fjord mouth more than 10 km from the SS terminus
345 (triangles in Fig. 7 a). We define ambient fjord waters as the average of these far-field CTD
346 profiles (red profile in Figs. 5 & 6).

347 Near the glacier we observe a range of water masses not found in the outer fjord. These
348 waters are generally colder, fresher, and more turbid than waters near the mouth of the fjord (Fig.
349 5 a, b). The REMUS sections reveal two distinct [Glacially Modified Waters \(GMW\)](#), which we
350 refer to as GMW1 and GMW2 (Fig. 4, Table 2). GMW1 and GMW2 are cold anomalies with a
351 high turbidity signal that are most evident at two distinct locations (Fig. 4). GMW1 is observed
352 in the southwestern ends of R1–R5 at ~40-m depth, while GMW2 is observed in the northeastern
353 ends of R1–R5 at ~60 m depth (Fig. 4). Both GMW1's and GMW2's temperature and turbidity
354 anomalies are most pronounced close to the glacier (Fig. 4 a–c), and decrease as these waters
355 spread away from the glacier (Fig. 4 g–i). For example, the high turbidity associated with
356 GMW1 spreads laterally beneath the pycnocline at R1 (Fig. 4 i). Turbidity does not consistently
357 map onto regions of local temperature minima; there are regions in the REMUS sections with
358 high turbidity but with temperatures above 0.9 °C (northeastern R1 below 80 m depth (Fig. 4 i)).
359 High turbidity in these regions may be due to other sources including suspended sediment
360 sourced from proglacial streams that enter SF as surface runoff near the northeastern end of R1
361 (Fig. 3) or iceberg discharge.

362 CTD casts 1–3 were taken closer to the SS face than the R5 transect during the same July
363 2012 field campaign (Fig. 3), and provide additional θ/S characteristics below the 100-m
364 REMUS depth limit (Fig. 6 a–c). These casts record deeper cold anomalies at the bottom of SF,
365 as well as cold excursions from ~40 to 80 m depth, similar to REMUS measurements (Fig. 6 a–
366 c). Overall the CTD profiles align well with REMUS measurements where coincident (above
367 100-m).

368 Further insight into the origins of GMW1 and GMW2 is found in θ/S space, where
369 GMW1 and GMW2 stand out as cold anomalies as compared to waters near the mouth of the
370 fjord (Figs. 5 d, 6 a, b). GMW1 and GMW2 are clustered at two distinct densities (Fig. 6 a, b).
371 At a density of $\sigma_θ \approx 24.8 \text{ kg m}^{-3}$, where $\sigma_θ$ is potential density less 1000 kg m^{-3} , GMW1 is lighter
372 than GMW2 ($\sigma_θ \approx 25.5 \text{ kg m}^{-3}$) (Table 2, Fig. 6 a, b). In general, GMW is fresher and more turbid
373 compared to ambient waters, consistent with fjord waters mixing with submarine melt and
374 subglacial discharge. If we assume that both GMW1 and GMW2 are driven by subglacial
375 discharge plumes that emerged at the grounding line, [then](#) we can assume that the bulk of the
376 entrainment was of deeper waters at densities of $\sigma_θ = 25.5$ –26.5 kg m^{-3} (Fig. 6 a, b). In θ/S space,
377 GMW is further identified with the use of meltwater and runoff mixing lines (Figs. 5 c, d & 6 a–
378 c), which represent conservative mixing between ambient water and submarine melt or
379 subglacial discharge, respectively (Jenkins, 1999). Endpoints for the melt and runoff mixing
380 lines are set to properties observed by CTD cast 2 at grounding line depth (Figs. 3, 6 b). GMW1
381 and GMW2 are consistent with the transformation of ambient waters by mixing with submarine
382 melt and subglacial discharge, as they fall between the meltwater and runoff mixing lines in θ/S
383 space (Fig. 5 c, d & 6 a–c).

384 Thus, near the glacier we observe water masses not found in the outer fjord that we
385 attribute to glacier/ocean interactions (Jenkins et al., 2010; Straneo et al., 2011). We observe two
386 distinct GMW that are both colder, fresher, and more turbid compared to ambient waters at
387 similar depths (Figs. 5 a–c, 6 a, b) but are located in different regions of the fjord (Fig. 3).

388 GMW1, observed in the southwestern ends of R1–R5, is considerably fresher and lighter than the
389 colder GMW2 observed in the northeastern ends of R1–R5 (Figs. 3, 6 a, b, Table 2). The lighter
390 GMW1 ($\sigma_0 \approx 24.8$) is observed at an equilibrium depth of 35–60 m, while the denser GMW2 (σ_0
391 ≈ 25.5) has a deeper equilibrium depth of 50–70 m (Table 2), suggesting that GMW1 contains a
392 higher fraction of subglacial runoff than GMW2 (See section 4.3). We further elucidate GMW1
393 and GMW2 origins in the following section on the SS catchment and subglacial discharge across
394 the SS terminus.

395

396 4.2. SS catchment and subglacial discharge across SS terminus

397 The $400 \pm 50 \text{ km}^2$ area SS catchment extends 15-km up the basal valley beneath the 6-km
398 wide SS outlet glacier snout and widens under inland ice, reaching a maximum inland extent of
399 35-km just above the 900 m a.s.l. ice-sheet surface elevation contour (Fig. 7 a, Table 3). Bedrock
400 basins that steer subglacial water to the southwest delineate the southern boundary of the
401 catchment (Fig. 7 a). The northern extent of the catchment is bounded by the Alángordliup
402 sermia outlet glacier catchment parallel to SS (Fig. 7 a). Three sub-catchments—C1, C2, and
403 C3—are delineated within the SS catchment from binning $-\nabla \Phi_h$ streamline endpoints along the
404 SS face in both the MBM2014 and BBM2013 analyses (Fig. 7 a). The main difference between
405 the MBM2014 and BBM2013 analyses is the size of the C1 subcatchment (BBM2013 33%

LAS 1/27/16 4:50 PM

Deleted: Observed

LAS 1/27/16 4:50 PM

Deleted: GMW1

LAS 1/27/16 4:50 PM

Deleted: amount

409 larger), with the BBM2013 analysis delineating the northern inland extent of C1 into a region the
410 MBM2014 analysis places in the Alángordliup sermia catchment (Figs. 1 & 7 a, Table 3).

411 The three sub-catchments delineate three sections along the terminus (Fig. 7 a), with each
412 section mapping onto a directly observed or inferred subglacial meltwater discharge channel
413 (D1, D2, and D3 in Fig. 3). Subcatchment C1, the largest sub-catchment at 269 km² area
414 (MBM2014) discharges along the middle of the terminus at discharge location D1, while
415 subcatchment C2 and C3 discharge along the northeastern and southwestern extents of the
416 terminus at D2 and D3, respectively (Fig. 3). D1 and D2 align with two distinct bathymetric
417 troughs of 150 and 132-m depth, respectively (Table 3), bounded by bathymetry highs of 60 to
418 40 meters depth in SF (Fig. 3). D1 and D2 also coincide with depressed glacier margin heights
419 along the terminus, enhanced ice sheet velocities (Joughin et al., 2013), and high calving flux
420 relative to the rest of the terminus. D1 is a particularly frequent calving region in comparison to
421 the rest of the terminus, as observed during our two field campaigns. At times, a turbulent,
422 sediment-rich plume reaches the fjord surface at D1, as observed in satellite images and during
423 subsequent fieldwork in July 2013 (Mankoff et al., [submitted](#)). While exhibiting similarly
424 frequent calving, terminus height, and velocity characteristics as D1, surface plumes have not
425 been observed at D2. Subcatchment C3 discharges beneath the slow-moving, southwestern
426 margin of the terminus at D3 (Fig. 3), through a visible, broad channel mouth at the fjord
427 surface, entering into a shallow region of SF (Table 3, Fig. 3).

428 Variability in calculated subglacial discharge for each subcatchment is controlled
429 primarily by temperature variability, with daily runoff rates a summation of melt and
430 precipitation across the catchment (van den Broeke et al., 2009) (Fig. 7 b, Table 3). During our
431 2012 field expedition, catchment runoff rates were slightly below the monthly July average, with

LAS 1/27/16 4:50 PM

Deleted: 2014

LAS 1/27/16 4:50 PM

Deleted: (Joughin et al., 2013)

434 no above average temperature days falling within the sampling period (Fig. 7 b). Disregarding
435 the possibility for periods of subglacial water storage during the en- and subglacial transport of
436 runoff to the SS terminus, daily discharge rates across the terminus during the field expedition
437 are $146 \text{ m}^3 \text{ s}^{-1}$ (MBM2014 estimate) (Table 3). An additional though likely minor amount of
438 surface meltwater runoff enters the fjord through proglacial streams, which discharge at land-
439 terminating margins abutting SS (Fig. 2). Daily runoff discharges for C1 and C2 scale primarily
440 with area differences and are 115.78 and $20.62 \text{ m}^3 \text{ s}^{-1}$, respectively (MBM2014) (Table 3). As
441 error estimates for the RACMO2.3 runoff rates are not available, we take the standard deviation
442 of July 2012 daily discharge rates as a measure of the potential variation observed during the
443 field expedition (Table 3).

444

445 **4.3. Buoyant plume model for the SS/SF system**

446 As described above, we have found evidence for three main subglacial catchments
447 discharging runoff into SF at three locations along the terminus. The two prominent discharge
448 locations, D1 and D2, coincide with GMW1 and GMW2 observations. The picture that emerges
449 is that different properties of GMW1 and GMW2 are attributable to differences in subglacial
450 discharge magnitude at that location. Here, we use a buoyant plume model to investigate the
451 extent to which the two plumes' predicted characteristics compare with the GMW1 and GMW2
452 observations. Buoyant plume theory states that the growth of a plume is dictated by the plume's
453 buoyancy forcing, which can be due to subglacial discharge at the grounding line and/or
454 submarine melting along the terminus (Morton et al., 1956; Turner, 1979). The buoyancy forcing
455 of the plume determines the plume's vertical velocity and entrainment of ambient fjord waters
456 (Morton et al., 1956; Turner, 1979). A class of simple, one-dimensional buoyant plume models

LAS 1/27/16 4:50 PM

Deleted: calculated

458 has been used to investigate plume dynamics and terminus melt rates near glaciers (Hellmer and
459 Olbers, 1989; Jenkins, 1991, 2011). Solutions to these models estimate plume temperature,
460 salinity, vertical velocity, width, and intrusion depth, the depth at which the plume becomes
461 neutrally buoyant and changes from flowing vertically up the terminus to flowing horizontally
462 away from the terminus. Here we investigate D1 and D2 plume scenarios using the Jenkins
463 (2011) buoyant plume model adapted to a half-conical plume driven by a point-source.

LAS 1/27/16 4:50 PM
Deleted: will use
LAS 1/27/16 4:50 PM
Deleted: investigate D1 and D2
LAS 1/27/16 4:50 PM
Deleted: scenarios
LAS 1/27/16 4:50 PM
Deleted: depth-integrated

464 The plume model uses conservation of the fluxes of mass, momentum, heat, and salt, to
465 calculate plume characteristics that are uniform in time and across-flow direction (Jenkins,
466 2011). Key initial conditions that we prescribe include an ice temperature of -10 °C (Lüthi et al.,
467 2002); fjord ambient temperature and stratification (Table 4); a vertical glacier face; and a
468 modeled subglacial discharge across the terminus, Q_{sg} (Table 4). Entrainment of ambient fjord
469 waters into the buoyant plume is modeled as a product of plume velocity, the sine of the ice
470 terminus slope (vertical for SS), and a theoretically defined entrainment coefficient (E_0) of 0.08
471 following Sciascia et al. (2013).

LAS 1/27/16 4:50 PM
Deleted: flux of
LAS 1/27/16 4:50 PM
Deleted: q_{sg}

472 The buoyant plume model is calculated for D1 and D2 scenarios and evaluated based on
473 end plume temperature, salinity, and intrusion depth (Table 4). Ambient water properties are
474 defined by two CTD measurements of full water column temperature and salinity from nearby
475 D1 and D2 (CTD1 and CTD2, respectively, in Fig. 3). Temperature, salinity, and intrusion depth
476 at the end of the plume are found to be largely insensitive to varying ambient fjord water
477 properties if the ambient waters show strong summer stratification. We use the RACMO2.3-
478 derived estimates of subglacial discharge across the terminus at D1 and D2 ($m^3 s^{-1}$) (using
479 MBM2014 of average daily runoff during the field expedition ($m^3 s^{-1}$)) (Table 3).

LAS 1/27/16 4:50 PM
Deleted: flux
LAS 1/27/16 4:50 PM
Deleted: m^2
LAS 1/27/16 4:50 PM
Deleted:) flowing through a 1-m vertical
slice of a theoretically calculated steady-state
Röthlisberger channel (Nye, 1976;
Röthlisberger, 1972; Schoof, 2010).

492 Given the observed ocean stratification and the modeled subglacial discharge, the plume
493 model confirms that GMW1 should be notably fresher and lighter ~~than~~ GMW2 (Fig. 5 c, Table
494 4). This supports the conclusion that GMW1 and GMW2 are the result of two distinct discharge
495 locations with different subglacial discharge magnitudes. ~~For the D2 scenario, the plume model~~
496 predicts ~~end~~ plume properties ~~and neutrally buoyant depths (~31 m)~~ that are ~~aligned with the~~
497 ~~GMW2 observations at similar depths (Fig. 5c, d). For the D1 scenario, the plume model predicts~~
498 ~~end plume properties that are~~ lighter and fresher than the observed ~~GMW1~~ (Fig. 5 c, Tables 2 &
499 4). The predicted D1 ~~plume~~ would reach ~~above~~ the ~~20-m-deep~~ pycnocline at neutral buoyancy
500 ~~depth of ~14 m~~ (Table 4). With a minimum amount of overshoot, we might expect the ~~D1 plume~~
501 to reach the surface or depths close enough to the surface to be visible during field observations.
502 In reality, the ~~plume at D1 was~~ not observed to reach the surface, and ~~GMW1~~ was only observed
503 beneath the pycnocline (Fig. 4). There are several possible reasons for this discrepancy. First, the
504 plume model may have an incorrect entrainment ~~parameterization~~. Second, the ~~estimated~~
505 subglacial discharge ~~could be~~ incorrect. In addition, after detaching from the terminus at the
506 plume's intrusion depth, GMW spreads an additional 150 m away from the SS face before being
507 observed at R5. Over this time, we would expect lateral mixing to further dilute the GMW
508 properties. The plume model does not describe lateral mixing, as the model ends when the plume
509 reaches intrusion depth.

510 511 5. Discussion

512 513 5.1. Subglacial catchments, discharge, and GMW observations

LAS 1/27/16 4:50 PM

Deleted: Following the steady-state solution for a single, hydrologically isolated Röthlisberger channel as derived by Slater et al. (2015), the relationship between the subglacial channel surface area, S , for a grounded tidewater glacier and subglacial discharge, Q_{sg} , is approximately $S \propto Q_{sg}^{6/7}$ (Slater et al., 2015). Following Slater et al. (2015), the effective pressure, N , for the D1 and D2 channel mouths is calculated using a water column depth of 150 m and an ice column thickness of 200 m. This results in a conduit size, S , of 37–92 m² for D1 and 9–21 m² for the D2. As channel mouth size and geometry have yet to be well observed at submerged glacier termini, we take the channel mouth geometry to be semi-circular, following observations of channel mouth geometries at land terminating glaciers (Fountain and Walder, 1998). The Jenkins (2011) model is uniform in the across-flow direction, thus the subglacial flux, q_{sg} , used for model simulations is the flux through a 1-m vertical slice ~~... [1]~~

LAS 1/27/16 4:50 PM

Deleted: that

LAS 1/27/16 4:50 PM

Deleted: In both scenarios

LAS 1/27/16 4:50 PM

Deleted: much

LAS 1/27/16 4:50 PM

Deleted: GMW

LAS 1/27/16 4:50 PM

Deleted: and D2 plumes

LAS 1/27/16 4:50 PM

Deleted: depths

LAS 1/27/16 4:50 PM

Deleted: 7 and ~10

LAS 1/27/16 4:50 PM

Deleted: respectively

LAS 1/27/16 4:50 PM

Deleted: plumes

LAS 1/27/16 4:50 PM

Deleted: plumes were

LAS 1/27/16 4:50 PM

Deleted: GMW

LAS 1/27/16 4:50 PM

Deleted: and/or submarine melt

LAS 1/27/16 4:50 PM

Deleted: prescribed subglacial flux, a function of

LAS 1/27/16 4:50 PM

Deleted: and channel surface area,

577 Our analysis of the ocean data and subglacial catchments both suggest that there are two
578 primary subglacial discharge locations along the ice/ocean interface. On the outlet glacier
579 catchment side of the interface, the primary subcatchments, C1 and C2 (Fig. 7a), route
580 substantial (>90%) of the total SS meltwater runoff (Table 3) into the fjord across the grounding
581 line at discharge locations D1 and D2, respectively (Fig. 3). On the ocean side of the interface,
582 GMW1 and GMW2 are located near D1 and D2, respectively, and show fresher, colder waters
583 with high turbidity as compared to ambient fjord waters (Fig. 5 a, b). The properties of these
584 waters, in particular, are consistent with glacial modification due to significant injection of
585 runoff at depth as is expected from a localized discharge of meltwater at D1 and D2. Finally,
586 between D1 and D2, there is a 2-km stretch of the terminus where GMW show cold excursions
587 with low to high turbidity along R4 and R5 (Fig. 6 c). The formation of this GMW is less clear,
588 though in this region between subglacial discharge locations, GMW properties are more
589 indicative of submarine melt and limited subglacial discharge and/or lateral mixing of GMW1
590 and GMW2.

591 Although we lack observations within the plumes themselves in 2012, the ocean
592 observations of GMW suggest that these waters are produced by ambient fjord waters interacting
593 with a limited number of discrete plumes along the terminus. Our observations of GMW beneath
594 the pycnocline at a distance of ~150 m from the terminus suggest that the two plumes reach
595 neutral buoyancy beneath the fjord surface. Visual observations during the 2012 field campaign
596 confirm that the plumes did not reach the fjord surface during this time. In contrast, during the
597 July 2013 field campaign at SF, a vigorous, turbulent plume was observed to break through at the
598 fjord surface at D1 (Mankoff et al., [submitted](#)).

LAS 1/27/16 4:50 PM
Deleted: 2014

600 Differences in subglacial discharge magnitude entering the fjord at D1 and D2 is both
601 observed and predicted to result in water mass differences between GMW1 and GMW2. Fed by
602 subglacial discharge from the largest subglacial subcatchment, GMW1 is fresher and lighter than
603 GMW2 (Table 3, Figs. 5 a-d, 6 a, b). D2 receives roughly 20% of the subglacial discharge
604 magnitude at D1 (Table 3). This smaller subglacial discharge results in a relatively saltier and
605 heavier GMW2 in comparison to GMW1 (Figs. 5 a-d, 6 a, b). While a greater volume of
606 subglacial discharge leads to a fresher water mass, the strength of the resultant buoyant plume
607 also plays a role in near-ice water mass transformation. Plume theory predicts that a plume fed
608 by a greater amount of subglacial discharge will have a stronger buoyancy forcing, leading to
609 both faster entrainment of ambient waters and an increase in the fraction of subglacial discharge
610 in the plume (Jenkins, 2011; Straneo and Cenedese, 2015). In this fjord, the entrainment of
611 ambient waters into a plume results in GMW with temperatures and salinities that are warmer
612 and saltier than the subglacial discharge entering the fjord ($\theta = 0$ °C, S = 0 PSU). The volume
613 fraction of entrained water for both D1 and D2 plumes is above 0.9 (Table 4), indicating that for
614 this fjord the plume temperature and salinity at neutral buoyancy depth are largely a function of
615 the entrained ambient water mass. Thus, overall, the greater subglacial discharge at D1 drives a
616 more vigorous plume that mixes with both IIW and SW, which results in GMW that is closer in
617 θ and S to SW than IIW (Table 2, Fig. 6 a). In contrast, smaller subglacial discharge at D2 drives
618 a less vigorous plume that mixes at deeper depths with only IIW, resulting in GMW that retains
619 the cold signature of subglacial discharge and submarine melting (Table 2, Fig. 6b).

620 Consistent with the ocean data, the plume model predicts end plume conditions at D1 are
621 fresher and lighter than those at D2 as they contain a greater amount of subglacial discharge (Fig.
622 5 d, Table 4). However, the end plume conditions from the Jenkins (2011) model for D1

LAS 1/27/16 4:50 PM

Deleted: a decrease

LAS 1/27/16 4:50 PM

Deleted: differences between GMW1

LAS 1/27/16 4:50 PM

Deleted: GMW2

LAS 1/27/16 4:50 PM

Deleted: consistent with plume theory, as GMW1 temperatures are closer to

LAS 1/27/16 4:50 PM

Deleted: fjord waters than the colder GMW2 (Fig. 6 a, b). Greater

LAS 1/27/16 4:50 PM

Deleted: and greater mixing

LAS 1/27/16 4:50 PM

Deleted: ambient fjord waters

LAS 1/27/16 4:50 PM

Deleted: Smaller

LAS 1/27/16 4:50 PM

Deleted: with less mixing with ambient fjord

waters

LAS 1/27/16 4:50 PM

Deleted: both

LAS 1/27/16 4:50 PM

Deleted: and D2

637 scenarios are lighter than the GMW1 we observe (Fig. 5 c, Table 4). In addition to errors in the
638 plume model and subglacial discharge estimates, lateral mixing within ~150 m of the terminus is
639 a consideration for comparing the plume model results and observed GMW. Large amounts of
640 mixing with ambient waters likely occur once the plume detaches from the terminus and GMW
641 is exported away from the ice/ocean interface. This lateral mixing has been observed in other
642 marine terminating outlet glacier systems in Greenland, where GMW from an inferred localized
643 subglacial discharge location was found uniformly across the fjord in profiles taken ~200 m from
644 the terminus (Chauché et al., 2014).

645

646 **5.2. Observing the heterogeneous near-ice environment**

647 The coupling of near-ice observations and subglacial discharge routing is necessary for
648 understanding ice-ocean interactions at marine terminating outlet glaciers. While multiple recent
649 studies have observed GMW in fjords (Chauché et al., 2014; Inall et al., 2014; Johnson et al.,
650 2011; Mortensen et al., 2011; Straneo et al., 2011; Sutherland et al., 2014) and others have
651 measured and modeled runoff based on surface catchment area (Mernild et al., 2015), no studies
652 have directly linked the two sides of this interface or considered the role of basal routing on
653 catchment area. For this study, we pair near-ice observations and subglacial discharge routing to
654 show for the first time that the observed GMW characteristics align with the subglacial discharge
655 magnitudes from outlet glacier subcatchments.

656 Our results highlight the necessity of subsurface observations within the near-ice zone for
657 accurately characterizing the heterogeneous processes at the ice/ocean interface. We observe
658 heterogeneous, subsurface GMW as high turbidity, cold excursions in across-fjord sections as far
659 as 1.5 km from the SS terminus (Fig. 4). Further away from the terminus, only the cold excursion

LAS 1/27/16 4:50 PM
Deleted: GMW
LAS 1/27/16 4:50 PM
Deleted: and even portions of the surface
waters of SF
LAS 1/27/16 4:50 PM
Deleted: Tables 2 &
LAS 1/27/16 4:50 PM
Deleted: flux
LAS 1/27/16 4:50 PM
Deleted: an additional

666 at the density of GMW1 remains in the far-field profiles (Fig. 5 d). Thus, while in the near-ice
667 zone there are multiple subglacial discharge locations across the SS grounding line and different
668 types of GMW observed, only a modified GMW1 is identifiable in far-field profiles. Noble gas
669 observations of GMW in neighboring Greenland fjords observe a dilution of GMW as you move
670 away from the terminus, suggesting that GMW is highly diluted outside of the near-ice zone
671 (Beard et al., 2015). Thus, the fact that only a modified GMW1 is detectable in the far-field
672 profiles is likely due to the larger volume flux of discharge from D1 entering the fjord as
673 compared to discharge from D2 (Table 4). Sill depth may be an additional factor impeding the
674 export of GMW2; GMW2 is observed at or barely above the 70-m sill depth, while GMW1 is
675 observed at shallower depths (Figs. 1 & 3, Table 2). The implication is that far-field
676 measurements only provide a partial representation of processes along the ice/ocean interface.

LAS 1/27/16 4:50 PM

Deleted: GMW1

LAS 1/27/16 4:50 PM

Deleted: GMW2

677 Similar to the single cold excursion observed in the ambient SF waters, many studies
678 have observed evidence of subsurface GMW uniformly distributed across fjord width outside of
679 the near-ice zone (Johnson et al., 2011; Mortensen et al., 2011; Straneo et al., 2011; Chauché et
680 al., 2014; Inall et al., 2014; Sutherland et al., 2014). Observations at Store and Rink glaciers as
681 close as ~200 m to termini identify one to a couple of surface and subsurface plumes along each
682 glacier termini (Chauché et al., 2014). However, the GMW observed 200 m from the termini is
683 uniform across the fjord (Chauché et al., 2014). While our observations of subglacial discharge
684 locations in SF are consistent with the low number of subglacial discharge locations found at
685 Store and Rink glaciers (Chauché et al., 2014), we are able to further differentiate and map types
686 of GMW to outlet glacier subcatchments.

687 The subsurface nature of the plumes and resultant GMW we observed is consistent with
688 multiple studies that have also observed subsurface GMW (Chauché et al., 2014; Inall et al.,

691 2014; Johnson et al., 2011; Mortensen et al., 2011; Straneo et al., 2011; Sutherland et al., 2014).
692 Together these findings drive home the point that plumes and other processes at the ice/ocean
693 interface actively driving submarine melt can and often do operate without creating an
694 expression on the fjord surface. Surface expressions of plumes have been detected at many
695 Greenland tidewater glaciers and invoked as evidence for runoff release from the ice sheet into
696 fjords and proglacial streams (Chu et al., 2009; Tedstone and Arnold, 2012), and have even been
697 proposed as a potentially useful remote measure of runoff variability (Chu et al., 2012).
698 However, our observations of plumes and GMW that reach neutral buoyancy beneath the
699 pycnocline suggest in many cases this relationship does not hold true. The magnitude of
700 subglacial discharge entering a fjord, fjord stratification, and fjord depth have all been shown to
701 affect whether a plume reaches the surface (Sciascia et al., 2013). The absence of plume surface
702 expression does not negate the presence of subglacial discharge plumes that may be driving
703 significant submarine melt and circulation along a tidewater terminus. Thus, across-fjord
704 subsurface observations within the near-ice zone provide the most comprehensive
705 characterization of ice/ocean interactions in Greenland fjords.

706

707 5.3. Observational constraints for modeling the heterogeneous near-ice environment

708 While spatial distribution of subglacial discharge is a critical component for estimating
709 submarine melt rates at marine terminating outlet glaciers in numerical models (Slater et al.,
710 2015), we have few observations to constrain subglacial discharge scenarios. Model
711 configurations of subglacial discharge for major Greenland outlet glaciers range from a
712 distributed subglacial system where equal amounts of subglacial discharge emerge across the
713 entire grounding line width (Jenkins, 2011; Sciascia et al., 2013), to partitioning subglacial

LAS 1/27/16 4:50 PM

Deleted: variability

LAS 1/27/16 4:50 PM

Deleted: amount

LAS 1/27/16 4:50 PM

Deleted: distributing

717 discharge between a number of equally-spaced plumes along the terminus (Kimura et al., 2014;
718 Slater et al., 2015), to routing all subglacial discharge through a single subglacial channel
719 emerging in one, central plume (Slater et al., 2015; Xu et al., 2013). While all these models,
720 which share the same melt parameterization, agree that submarine melt rates increase with
721 increasing subglacial discharge (Jenkins, 2011; Kimura et al., 2014; Sciascia et al., 2013; Slater
722 et al., 2015; Xu et al., 2012, 2013), the amount and distribution of the increased melting depends
723 on the largely unknown pattern of subglacial discharge (Straneo and Cenedese, 2015). Most
724 recently, Slater et al. (2015) concluded that a distributed system yields as much as 5 times more
725 submarine melting than a channelized system consisting of a few plumes along the terminus.
726 Thus, spatial distribution of subglacial melt is critically important for accurately estimating
727 submarine melt rates in a numerical model (Slater et al., 2015; Straneo and Cenedese, 2015).

LAS 1/27/16 4:50 PM

Deleted: All

728 For this system, we observe at least two, localized areas of subglacial discharge separated
729 by wide areas of the terminus with little to no subglacial discharge. Our survey interval was
730 limited to peak summer conditions, when one would expect channelized subglacial discharge.
731 Observations during other times of the year, in particular prior to and during the onset of
732 meltwater runoff early in the melt season, as well as towards the end of the melt season when
733 runoff is reduced again, would be useful to more fully characterize the seasonally evolving
734 magnitude and type of subglacial discharge in this environment. A simple subglacial meltwater
735 routing model using MBM2014, the GIMP ice sheet surface digital elevation model, and
736 RACMO2.3 runoff estimates was able to predict the number, approximate location, and relative
737 magnitude and type of subglacial discharge locations. And while this subglacial catchment
738 delineation method should be supplemented with ocean measurements and field observations
739 where possible, in many cases it may prove a useful first order approximation of the spatial

LAS 1/27/16 4:50 PM

Deleted: (Slater et al., 2015).

742 distribution of subglacial discharge at other marine terminating outlet glaciers where fjord
743 observations are lacking or difficult to obtain.

744

745 **6. Conclusions**

746 Hydrographic surveys completed by an AUV in Sarqardleq Fjord provide several new
747 observational insights to the characteristics and distribution of near-ice GMW in a shallow-silled,
748 moderate-sized west Greenland fjord. Overcoming navigation difficulties in the acoustically
749 noisy, iceberg-filled fjord, the AUV covered a large portion of the near-ice waters along the
750 terminus. AUV observations provide the most comprehensive and spatiotemporally detailed
751 snapshots of across-fjord hydrography in the near-ice zone to date. From these measurements we
752 identified two types of GMW that map onto two plumes based on θ /S/turbidity near-ice
753 properties and subcatchment runoff estimates. The two plumes are, notably, not observed to
754 reach the surface in the fjords, but attain neutral buoyancy beneath the pycnocline of the strongly
755 stratified summer fjord conditions.

756 Our observations detail how mixing processes at the ice/ocean interface driven by either
757 submarine melting and/or plumes fed by subglacial discharge can produce GMW that is colder,
758 fresher, and at times more turbid than ambient fjord waters. An idealized plume model for
759 plumes fed by a range of RACMO2.3-derived subglacial discharges appropriate for the two
760 plumes observed in this fjord is qualitatively consistent with the largest subglacial discharge
761 being associated with the lighter, fresher glacially modified watermass. The characterization of
762 GMW and subglacial catchments for this outlet glacier system provides critical observational
763 constraints on the widely varying subglacial discharge scenarios employed by the current set of
764 submarine melt modeling studies. Results supply near-ice observations abutting one Greenland

LAS 1/27/16 4:50 PM
Deleted: fluxes

LAS 1/27/16 4:50 PM
Deleted: flux

767 Ice Sheet outlet glacier, though the continued investigation of other Greenland outlet glaciers is
768 much needed to ultimately move towards an accurate representation of oceanic forcing at outlet
769 glacier termini and an improved understanding of the ice sheet's outlet glacier dynamics.

770 **Acknowledgements**

771 Support was provided by the National Science Foundation's Office of Polar Programs (NSF-
772 OPP) through PLR-1418256 to F.S., S.B.D. and A.J.P., PLR-1023364 to S.B.D., and through the
773 Woods Hole Oceanographic Institution Ocean and Climate Change Institute Arctic Research
774 Initiative to F.S., S.B.D., and A.J.P. L.A.S. was also supported by a National Science Foundation
775 Graduate Research Fellowship. S.B.D was also supported by the Woods Hole Oceanographic
776 Institution James E. and Barbara V. Moltz Research Fellowship. M.M. was supported by the
777 National Aeronautics and Space Administration's (NASA) Cryospheric Sciences Program
778 through NNX15AD55G. The authors would like to acknowledge Michiel van den Broeke for
779 providing RACMO output; Jeff Pietro and John Kemp of the WHOI Mooring Operations,
780 Engineering and Field Support Group, and Rebecca H. Jackson and Ove Villadsen for their help
781 during the 2012 field operations; Clark Richards for guidance using the Barnes Objective
782 Analysis; Kenneth D. Mankoff for conversations on plumes in Sarqardleq Fjord; Nicholas L.
783 Baird for conversations on glacially modified waters in Greenland fjords; and Adrian Jenkins
784 and [Claudia Cenedese](#) for [providing](#) the plume model code [and discussing its application](#).
785

786 **Author contributions**

787 F.S., S.B.D., and A.J.P. conceived the study. F.S., S.B.D., and A.L.K. performed the fieldwork.
788 A.J.P., A.L.K., and L.A.S. processed the REMUS data. [L.A.S.](#), F.S., S.B.D., and A.J.P. analyzed
789 the REMUS and CTD data. L.A.S. created the bathymetry map. M.M. provided the reprocessed
790 [bedrock elevation map](#). L.A.S., F.S., S.B.D., and A.J.P. interpreted the results. L.A.S. wrote the
791 paper. All authors commented on the paper.

792

793 **Competing financial interests**

794 The authors declare no competing financial interests.

795

796 **References**

797 Andrews, L. C., Catania, G. A., Hoffman, M. J., Gulley, J. D., Lüthi, M. P., Ryser, C., Hawley,
798 R. L. and Neumann, T. A.: Direct observations of evolving subglacial drainage beneath the
799 Greenland Ice Sheet, *Nature*, 514(7520), 80–83, doi:10.1038/nature13796, 2014.

800 Bamber, J., van den Broeke, M., Ettema, J., Lenaerts, J. and Rignot, E.: Recent large increases in
801 freshwater fluxes from Greenland into the North Atlantic, *Geophys. Res. Lett.*, 39(19), 1–4,
802 doi:10.1029/2012GL052552, 2012.

803 Bamber, J. L., Griggs, J. a., Hurkmans, R. T. W. L., Dowdeswell, J. a., Gogineni, S. P., Howat,
804 I., Mouginot, J., Paden, J., Palmer, S., Rignot, E. and Steinhage, D.: A new bed elevation dataset
805 for Greenland, *Cryosph.*, 7(2), 499–510, doi:10.5194/tc-7-499-2013, 2013.

806 Banwell, A. F., Willis, I. C. and Arnold, N. S.: Modeling subglacial water routing at Paakitsoq,
807 W Greenland, *J. Geophys. Res. Earth Surf.*, 118(3), 1282–1295, doi:10.1002/jgrf.20093, 2013.

808 Barnes, S. L.: Applications of the Barnes Objective Analysis Scheme. Part I: Effects of
809 Undersampling, Wave Position, and Station Randomness, *J. Atmos. Ocean. Technol.*, 11, 1433–
810 1448, 1994.

811 Beaird, N., Straneo, F. and Jenkins, W.: [Spreading of Greenland meltwaters in the ocean revealed by noble gases](#), *Geophys. Res. Lett.*, 42, doi:10.1002/2015GL065003, 2015.

812

813 Box, J. E., Yang, L., Bromwich, D. H. and Bai, L.-S.: Greenland Ice Sheet Surface Air
814 Temperature Variability: 1840–2007*, *J. Clim.*, 22(14), 4029–4049,
815 doi:10.1175/2009JCLI2816.1, 2009.

816 Van den Broeke, M., Bamber, J., Ettema, J., Rignot, E., Schrama, E., van de Berg, W. J., van
817 Meigaard, E., Velicogna, I. and Wouters, B.: Partitioning recent Greenland mass loss., *Science*,
818 326(5955), 984–986, doi:10.1126/science.1178176, 2009.

819 Chandler, D. M., Wadham, J. L., Lis, G. P., Cowton, T., Sole, A., Bartholomew, I., Telling, J.,
820 Nienow, P., Bagshaw, E. B., Mair, D., Vinen, S. and Hubbard, A.: Evolution of the subglacial
821 drainage system beneath the Greenland Ice Sheet revealed by tracers, *Nat. Geosci.*, 6(4), 1–4,
822 2013.

823 Chauché, N., Hubbard, A., Gascard, J. C., Box, J. E., Bates, R., Koppes, M., Sole, A.,
824 Christoffersen, P. and Patton, H.: Ice–ocean interaction and calving front morphology at two
825 west Greenland tidewater outlet glaciers, *Cryosph.*, 8(4), 1457–1468, doi:10.5194/tc-8-1457-
826 2014, 2014.

827 Chu, V. W., Smith, L. C., Rennermalm, A. K., Forster, R. R. and Box, J. E.: Hydrologic controls
828 on coastal suspended sediment plumes around the Greenland ice sheet, *Cryosph. Discuss.*, 5,
829 2365–2407, doi:10.5194/tcd-5-2365-2011, 2012.

LAS 1/27/16 4:50 PM

Deleted: Noble Gases Trace Greenland's Surface and Submarine Melt

LAS 1/27/16 4:50 PM

Deleted: Ocean, Submitted

833 Chu, V. W., Smith, L. C., Rennermalm, A. K., Forster, R. R., Box, J. E. and Reehy, N.: Sediment
834 plume response to surface melting and supraglacial lake drainages on the Greenland ice sheet, *J.*
835 *Glaciol.*, 55, 1072–1082, doi:10.3189/002214309790794904, 2009.

836 Cuffey, K. M. and Patterson, W. S. B.: *The Physics of Glaciers*, 4th ed., Elsevier., 2010.

837 Enderlin, E., Howat, I. M. and Jeong, S.: An improved mass budget for the Greenland ice sheet,
838 *Geophys. Res. Lett.*, 41, 866–872, doi:10.1002/2013GL059010, 2014.

839 Fountain, A. G. and Walder, J. S.: Water flow through temperate glaciers, *Rev. Geophys.*,
840 36(97), 299, doi:10.1029/97RG03579, 1998.

841 Gladish, C., Holland, D. M., Rosing-Asvid, A., Behrens, J. W. and Boje, J.: Oceanic Boundary
842 Conditions for Jakobshavn Glacier. Part I: Variability and Renewal of Ilulissat Icefjord Waters,
843 2001–14, *J. Phys. Oceanogr.*, doi:10.1175/JPO-D-14-0044.1, 2015a.

844 Gladish, C. V., Holland, D. M. and Lee, C. M.: Oceanic Boundary Conditions for Jakobshavn
845 Glacier. Part II: Provenance and Sources of Variability of Disko Bay and Ilulissat Icefjord
846 Waters, 1990- 2011, *J. Phys. Oceanogr.*, 45(2003), 33–63, doi:10.1175/JPO-D-14-0045.1,
847 2015b.

848 Hellmer, H. H. and Olbers, D. J.: A two-dimensional model for the thermohaline circulation
849 under an ice shelf, *Antarct. Sci.*, 1(4), 325–336, doi:10.1017/S0954102089000490, 1989.

850 Hewitt, I. J., Schoof, C. and Werder, M. A.: Flotation and free surface flow in a model for
851 subglacial drainage. Part 2. Channel flow, *J. Fluid Mech.*, 702, 157–187.

852 Holland, D. M., Thomas, R. H., de Young, B., Rønne, M. H. and Lyberth, B.: Acceleration
853 of Jakobshavn Isbræ triggered by warm subsurface ocean waters, *Nat. Geosci.*, 1(10), 659–664,
854 doi:10.1038/ngeo316, 2008.

855 Howat, I. M., Negrete, A. and Smith, B. E.: The Greenland Ice Mapping Project (GIMP) land
856 classification and surface elevation data sets, *Cryosph.*, 8, 1509–1518, doi:10.5194/tc-8-1509-
857 2014, 2014.

858 Inall, M. E., Murray, T., Cottier, F. R., Scharrer, K. and Boyd, T. J.: Oceanic heat delivery via
859 Kangerdlugssuaq Fjord to the south-east Greenland ice sheet, *J. Geophys. Res. Ocean.*, 119,
860 631–645, doi:10.1002/2013JC009295, 2014.

861 Jackson, R. H., Straneo, F. and Sutherland, D. A.: Externally forced fluctuations in ocean
862 temperature at Greenland glaciers in non-summer months, *Nat. Geosci.*, 1–6,
863 doi:10.1038/ngeo2186, 2014.

864 Jenkins, A.: A one-dimensional model of ice shelf-ocean interaction, *J. Geophys. Res.*, 96(C11),
865 671–677, 1991.

866 Jenkins, A.: The Impact of Melting Ice on Ocean Waters, *J. Phys. Oceanogr.*, 29, 2370–2381,
867 1999.

868 Jenkins, A.: Convection-Driven Melting near the Grounding Lines of Ice Shelves and Tidewater
869 Glaciers, *J. Phys. Oceanogr.*, 41(12), 2279–2294, doi:10.1175/JPO-D-11-03.1, 2011.

870 Jenkins, A., Dutrieux, P., Jacobs, S. S., McPhail, S. D., Perrett, J. R., Webb, A. T. and White, D.:
871 Observations beneath Pine Island Glacier in West Antarctica and implications for its retreat, *Nat.*
872 *Geosci.*, 3(7), 468–472, doi:10.1038/ngeo890, 2010.

873 Johnson, H. L., Münchow, A., Falkner, K. K. and Melling, H.: Ocean circulation and properties
874 in Petermann Fjord, Greenland, *J. Geophys. Res. Ocean.*, 116, 1–18,
875 doi:10.1029/2010JC006519, 2011.

876 Joughin, I., Alley, R. B. and Holland, D. M.: Ice-Sheet Response to Oceanic Forcing, *Science*,
877 338, 1172–1176, 2012.

878 Joughin, I., Das, S. B., Flowers, G. E., Behn, M. D., Alley, R. B., King, M. A., Smith, B. E.,
879 Bamber, J. L., van den Broeke, M. R. and van Angelen, J. H.: Influence of ice-sheet geometry
880 and supraglacial lakes on seasonal ice-flow variability, *Cryosph.*, 7(4), 1185–1192, 2013.

881 Kimura, S., Holland, P. R., Jenkins, A. and Piggott, M.: The Effect of Meltwater Plumes on the
882 Melting of a Vertical Glacier Face, *J. Phys. Oceanogr.*, 140917134924005, doi:10.1175/JPO-D-
883 13-0219.1, 2014.

884 Lewis, S. M. and Smith, L. C.: Hydrologic drainage of the Greenland Ice Sheet, *Hydrol.*
885 *Process.*, 23, 2004–2011, doi:10.1002/hyp, 2009.

886 Lüthi, M., Funk, M., Gogineni, S. and Truffer, M.: Mechanisms of fast flow in Jakobshavn
887 Isbræ, Greenland, Part III. Measurements of ice deformation, temperature and cross-borehole
888 conductivity in boreholes to the bedrock, *J. Glaciol.*, 48(162), 369–385, 2002.

889 Mankoff, K. D., Straneo, F., [Cenedese, C.](#), Das, S. B., [Richards, C. G.](#), and [Singh, H.](#): [Structure](#)
890 [and dynamics of a subglacial plume in a Greenland fjord, submitted J. Geophys. Res.](#)

891 Mernild, S. H., Holland, D. M., Holland, D., Rosing-Asvid, A., Yde, J. C., Liston, G. E. and
892 Steffen, K.: Freshwater Flux and Spatiotemporal Simulated Runoff Variability into Ilulissat
893 Icefjord, West Greenland, Linked to Salinity and Temperature Observations near Tidewater
894 Glacier Margins Obtained Using Instrumented Ringed Seals, *J. Phys. Oceanogr.*, 45, 1426–1445,
895 doi:10.1175/JPO-D-14-0217.1, 2015.

896 Moon, T. and Joughin, I.: Changes in ice front position on Greenland's outlet glaciers from 1992
897 to 2007, *J. Geophys. Res.*, 113(F2), F02022, doi:10.1029/2007JF000927, 2008.

898 Morlighem, M., Rignot, E., Mouginot, J., Seroussi, H. and Larour, E.: Deeply incised submarine
899 glacial valleys beneath the Greenland ice sheet, *Nat. Geosci.*, 7, 18–22, doi:10.1038/ngeo2167,
900 2014.

901 Mortensen, J., Lennert, K., Bendtsen, J. and Rysgaard, S.: Heat sources for glacial melt in a sub-
902 Arctic fjord (Godthåbsfjord) in contact with the Greenland Ice Sheet, *J. Geophys. Res.*, 116,
903 doi:10.1029/2010JC006528, 2011.

904 Morton, B. R., Taylor, G. and Turner, J. S.: Turbulent Gravitational Convection from Maintained
905 and Instantaneous Sources, *Proc. R. Soc. A Math. Phys. Eng. Sci.*, 234(1196), 1–23,
906 doi:10.1098/rspa.1956.0011, 1956.

907 Moteika, R. J., Dryer, W. P., Amundson, J., Truffer, M. and Fahnestock, M.: Rapid submarine
908 melting driven by subglacial discharge, LeConte Glacier, Alaska, *Geophys. Res. Lett.*, 40(19),
909 5153–5158, doi:10.1002/grl.51011, 2013.

910 Nye, J. F.: Water flow in glaciers: jökulhlaups, tunnels and veins, *J. Glaciol.*, 17, 181–207, 1976.

911 Palmer, S., Shepherd, A., Nienow, P. and Joughin, I.: Seasonal speedup of the Greenland Ice
912 Sheet linked to routing of surface water, *Earth Planet. Sci. Lett.*, 302, 423–428,
913 doi:10.1016/j.epsl.2010.12.037, 2011.

914 Plueddemann, A. J., Kukulya, A. L., Stokey, R. and Freitag, L.: Autonomous Underwater
915 Vehicle Operations Beneath Coastal Sea Ice, *IEEE/ASME Trans. Mechatronics*, 17(1), 54–64,
916 2012.

917 Post, A., O’Neil, S., Moteika, R. and Streveler, G.: A Complex Relationship Between Calving
918 Glaciers and Climate, *EOS Trans.*, 92(37), 305–312, 2011.

919 Rignot, E. and Kanagaratnam, P.: Changes in the velocity structure of the Greenland Ice Sheet,
920 *Science*, 311, 986–990, doi:10.1126/science.1121381, 2006.

921 Röthlisberger, H.: Water pressure in intra- and subglacial channels, *J. Glaciol.*, 11(62), 177–203,
922 1972.

923 Schoof, C.: Ice-sheet acceleration driven by melt supply variability, *Nature*, 468(7325), 803–806,
924 2010.

925 Schumann, K., Völker, D. and Weinrebe, W. R.: Acoustic mapping of the Ilulissat Ice Fjord
926 mouth, West Greenland, *Quat. Sci. Rev.*, 40, 78–88, doi:10.1016/j.quascirev.2012.02.016, 2012.

927 Sciascia, R., Straneo, F., Cenedese, C. and Heimbach, P.: Seasonal variability of submarine melt
928 rate and circulation in an East Greenland fjord, *J. Geophys. Res. Ocean.*, 118, 2492–2506,
929 doi:10.1002/jgrc.20142, 2013.

930 Shepherd, A., Ivins, E. R., A, G., Barletta, V. R., Bentley, M. J., Bettadpur, S., Briggs, K. H.,
931 Bromwich, D. H., Forsberg, R., Galin, N., Horwath, M., Jacobs, S., Joughin, I., King, M. A.,
932 Lenaerts, J. T. M., Li, J., Ligtenberg, S. R. M., Luckman, A., Luthcke, S. B., McMillan, M.,
933 Meister, R., Milne, G., Mouginot, J., Muir, A., Nicolas, J. P., Paden, J., Payne, A. J., Pritchard,
934 H., Rignot, E., Rott, H., Sorensen, L. S., Scambos, T. A., Scheuchl, B., Schrama, E. J. O., Smith,
935 B., Sundal, A. V., van Angelen, J. H., van de Berg, W. J., van den Broeke, M. R., Vaughan, D.
936 G., Velicogna, I., Wahr, J., Whitehouse, P. L., Wingham, D. J., Yi, D., Young, D. and Zwally, H.
937 J.: A Reconciled Estimate of Ice-Sheet Mass Balance, *Science*, 338(6111), 1183–1189, 2012.

938 Shreve, R. L.: Movement of water in glaciers, *J. Glaciol.*, 11(62), 205–214, 1972.

939 Slater, D. A., Nienow, P. W., Cowton, T. R., Goldberg, D. N. and Sole, A. J.: Effect of near-
940 terminus subglacial hydrology on tidewater, *Geophys. Res. Lett.*, 42, 1–8,
941 doi:10.1002/2014GL062494.1, 2015.

942 Straneo, F. and Cenedese, C.: The Dynamics of Greenland's Glacial Fjords and Their Role in
943 Climate, *Ann. Rev. Mar. Sci.*, 7, 89–112, doi:10.1146/annurev-marine-010213-135133, 2015.

944 Straneo, F., Curry, R. G., Sutherland, D. a., Hamilton, G. S., Cenedese, C., Våge, K. and Stearns,
945 L. a.: Impact of fjord dynamics and glacial runoff on the circulation near Helheim Glacier, *Nat.*
946 *Geosci.*, 4, 322–327, doi:10.1038/ngeo1109, 2011.

947 Straneo, F., Hamilton, G. S., Sutherland, D. A., Stearns, L. A., Davidson, F., Hammill, M. O.,
948 Stenson, G. B. and Rosing-Asvid, A.: Rapid circulation of warm subtropical waters in a major
949 glacial fjord in East Greenland, *Nat. Geosci.*, 3, 182–186, doi:10.1038/ngeo764, 2010.

950 Straneo, F. and Heimbach, P.: North Atlantic warming and the retreat of Greenland's outlet
951 glaciers., *Nature*, 504(7478), 36–43, doi:10.1038/nature12854, 2013.

952 Straneo, F., Heimbach, P., Sergienko, O., Hamilton, G., Catania, G., Griffies, S., Hallberg, R.,
953 Jenkins, A., Joughin, I., Motyka, R., Pfeffer, W. T., Price, S. F., Rignot, E., Scambos, T., Truffer,
954 M. and Vieli, A.: Challenges to Understanding the Dynamic Response of Greenland's Marine
955 Terminating Glaciers to Oceanic and Atmospheric Forcing, *Bull. Am. Meteorol. Soc.*, 94(8),
956 1131–1144, doi:10.1175/BAMS-D-12-00100.1, 2013.

957 Sutherland, D. A., Straneo, F. and Pickart, R. S.: Characteristics and dynamics of two major
958 Greenland glacial fjords, *J. Geophys. Res. Ocean.*, 119, 3767–3791, doi:10.1002/jgrc.20224,
959 2014.

960 Tedstone, A. J. and Arnold, N. S.: Automated remote sensing of sediment plumes for
961 identification of runoff from the Greenland ice sheet, *J. Glaciol.*, 58(210), 699–712,
962 doi:10.3189/2012JoG11J204, 2012.

963 Thomas, R., Frederick, E., Krabill, W., Manizade, S. and Martin, C.: Recent changes on
964 greenland outlet glaciers, *J. Glaciol.*, 55(189), 147–162, doi:10.3189/002214309788608958,
965 2009.

966 Turner, J. S.: Buoyancy effects in fluids, Cambridge University Press., 1979.

967 Van den Broeke, M., Bamber, J., Ettema, J., Rignot, E., Schrama, E., van de Berg, W. J., van
968 Meijgaard, E., Velicogna, I. and Wouters, B.: Partitioning recent Greenland mass loss., *Science*,
969 326(5955), 984–986, doi:10.1126/science.1178176, 2009.

970 Werder, M. A., Hewitt, I. J., Schoof, C. G. and Flowers, G. E.: Modeling channelized and
971 distributed subglacial drainage in two dimensions, *J. Geophys. Res. Earth Surf.*, 118(4), 2140–
972 2158, doi:10.1002/jgrf.20146, 2013.

973 Xu, Y., Rignot, E., Fenty, I., Menemenlis, D. and Flexas, M. M.: Subaqueous melting of Store
974 Glacier, west Greenland from three-dimensional, high-resolution numerical modeling and ocean
975 observations, *Geophys. Res. Lett.*, 40(17), 4648–4653, doi:10.1002/grl.50825, 2013.

976 Xu, Y., Rignot, E., Menemenlis, D. and Koppes, M.: Numerical experiments on subaqueous
977 melting of Greenland tidewater glaciers in response to ocean warming and enhanced subglacial
978 discharge, *Ann. Glaciol.*, 53(60), 1–6, doi:10.3189/2012/AoG60A139, 2012.

979
980**Table 1: REMUS Missions in Sarqardleq Fjord**

Mission	Date	Local Time at Mission Start	Duration (h:mm)	Transect Sampling Path (m- depth)	Distance Traveled (km)
R1	7/18	21:10	1:28	Yo-Yo = 5–90	9.00
R2	7/21	15:37	3:41	Yo-Yo = 5–50; Fixed Depth=50, 70; Altitude = 10 m off bottom	23.11
R3	7/22	14:58	6:25	Yo-Yo = 5–55; Fixed Depth= 60, 70; Altitude = 10 m above bottom	41.36
R4	7/23	14:37	5:05	Yo-Yo = 5–50; Fixed Depth = 60, 70; Altitude = 10 m above bottom	30.93
R5	7/24	18:12	5:26	Yo-Yo 5–60; Fixed Depth=40, 55, 70; Altitude = 10 m above bottom	34.91

981

982

983 **Table 2: Water mass properties in Sarqardleq Fjord**

984

Water mass	Surface Water (SW)	Ilulissat Icefjord Waters (IIW)	Glacially Modified Water 1 (GMW1)	Glacially Modified Water 2 (GMW2)
Depth range (m)	0–20	20–SF bottom	35–60	50–70
S (PSU)	21–30.5	32.5–33.5	30.8–31.5	31.1–32.3
θ (°C)	1.5–10	0.8–1.5	0.75–0.85	0.59–0.75
σ_0 ($\rho_0 - 1000$ kg m $^{-3}$)	16.0–24.3	25.9–26.7	24.6–25.1	24.8–25.8
Turbidity (NTU)	Low (<4 NTU)	Low (<4 NTU)	High (>9 NTU)	High (>9 NTU)
Origin/Formation	Local formation	Disko and Baffin Bay	Local formation	Local formation

985

986

Table 3: Sarqardliup sermia subcatchments and runoff estimates

Subcatchment	C1	C2	C3	SS ($\sum C1-3$)
Discharge location	D1	D2	D3	--
Bathymetry along catchment terminus				
Average depth (m)	116.4	101.5	39.9	--
Maximum depth (m)	150.4	131.8	49.9	--
<i>Morlighem et al. (2014) (MBM2014)</i>				
Catchment area (km^2)	268.74	47.97	23.31	340.02
Catchment area compared to SS (%)	79%	14%	7%	--
Catchment average daily runoff July 2012 $\pm \sigma_{JULY}(Q_{sg})$ ($\text{m}^3 \text{s}^{-1}$)	115.78 \pm 42.59	20.62 \pm 7.33	9.97 \pm 3.47	146.37 \pm 53.26
Average daily July runoff compared to SS (%)	79%	14%	7%	--
Catchment average daily runoff during the field expedition (DOY 200, 203–206) $\pm \sigma_{JULY}(Q_{sg})$ ($\text{m}^3 \text{s}^{-1}$)	88.70 \pm 42.59	16.10 \pm 7.33	7.89 \pm 3.47	112.69 \pm 53.26
<i>Bamber et al. (2013) (BBM2013)</i>				
Catchment area (km^2)	402	42	9	453
Catchment area compared to SS (%)	89%	9%	2%	--
Catchment average daily runoff July 2012 $\pm \sigma_{JULY}(Q_{sg})$ ($\text{m}^3 \text{s}^{-1}$)	171.01 \pm 64.27	17.47 \pm 6.40	3.72 \pm 1.36	192.20 \pm 71.75
Average daily July runoff compared to SS (%)	89%	9%	2%	--
Catchment average daily runoff during the field expedition (DOY 200, 203–206) $\pm \sigma_{JULY}(Q_{sg})$ ($\text{m}^3 \text{s}^{-1}$)	122.83 \pm 64.27	14.08 \pm 6.40	3.05 \pm 1.36	139.96 \pm 71.75

991 | Table 4. **Buoyant** plume model simulations for D1 and D2 scenarios at MBM2014
 992 | subglacial discharge values. Plume θ and S ranges are plotted in Fig. 5 c, d.

	D1	D2
Ambient θ/S profile	CTD 1	CTD 2
Calving face depth (m)	153	140
Subglacial <u>Discharge (Q_{sg}) (m³ s⁻¹)</u>	[46.11, 88.70, 131.29]	[8.77, 16.10, 23.43]
Plume θ (°C) <u>at neutral buoyancy depth</u>	[0.82, 0.85, 0.84]	[0.83, 0.82, 0.82]
Plume S (PSU) <u>at neutral buoyancy</u> <u>depth</u>	[30.50, 29.72, 29.17]	[31.32, 30.88, 30.56]
Plume σ_0 ($\rho_0 - 1000 \text{ kg m}^{-3}$) <u>at neutral</u> <u>buoyancy depth</u>	[24.34, 23.74, 23.30]	[24.90, 24.59, 24.35]
Neutral buoyancy depth (m)	[21.79, 14.03, 13.79]	[41.41, 31.23, 27.68]
Volume <u>fraction of entrained water</u>	[0.94, 0.94, 0.94]	[0.96, 0.96, 0.96]

994

995

LAS 1/27/16 4:50 PM

Deleted: 1-D buoyant

LAS 1/27/16 4:50 PM

Deleted: 5c

LAS 1/27/16 4:50 PM

Deleted: Channel mouth surface area ... [2]

LAS 1/27/16 4:50 PM

Deleted: Flux (q_{sg}) (m²)

LAS 1/27/16 4:50 PM

Deleted: [5.99, 8.71, 10.90]

LAS 1/27/16 4:50 PM

Deleted: [2.32, 3.28, 4.07]

LAS 1/27/16 4:50 PM

Deleted:

LAS 1/27/16 4:50 PM

Deleted: 60

LAS 1/27/16 4:50 PM

Deleted: 56

LAS 1/27/16 4:50 PM

Deleted: 54

LAS 1/27/16 4:50 PM

Deleted: 69

LAS 1/27/16 4:50 PM

Deleted: 67

LAS 1/27/16 4:50 PM

Deleted: 64

LAS 1/27/16 4:50 PM

Deleted: 24.51, 22.92, 21.87

LAS 1/27/16 4:50 PM

Deleted: 27.91, 26.59, 25

LAS 1/27/16 4:50 PM

Deleted: [19.54, 18.27, 17.43]

LAS 1/27/16 4:50 PM

Deleted: [22.26, 21.20, 20.64]

LAS 1/27/16 4:50 PM

Deleted: 7.15, 7.12, 7.16

LAS 1/27/16 4:50 PM

Deleted: 9.75, 9.88, 9.08

LAS 1/27/16 4:50 PM

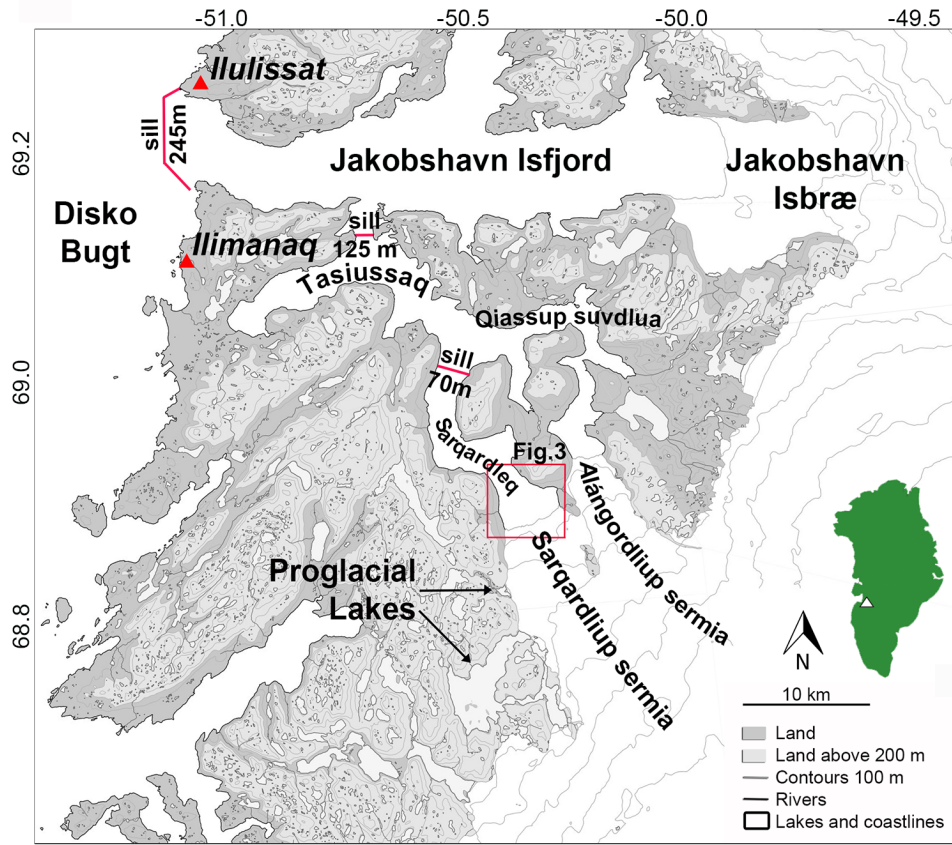
Deleted: flux (V_f) (m² s⁻¹)

LAS 1/27/16 4:50 PM

Deleted: [24.73, 29.88, 33.65]

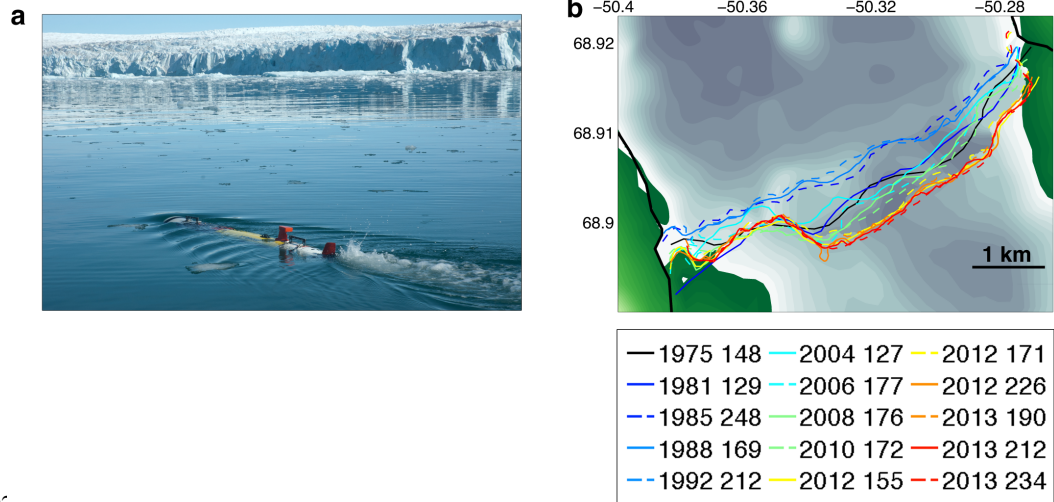
LAS 1/27/16 4:50 PM

Deleted: [15.71, 18.34, 20.34]

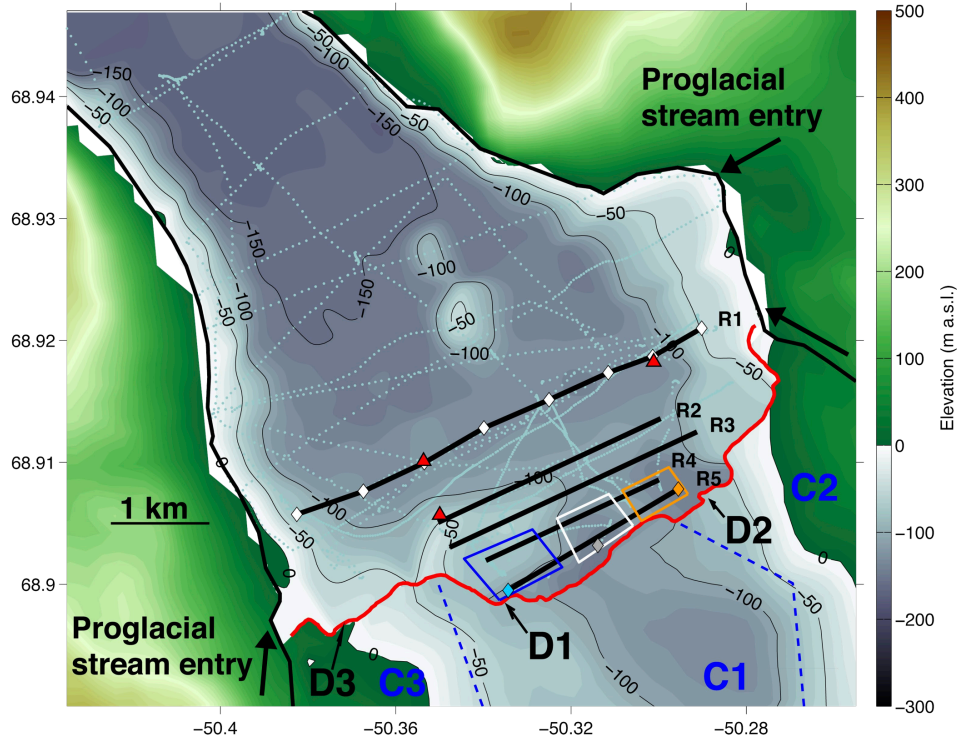


1018

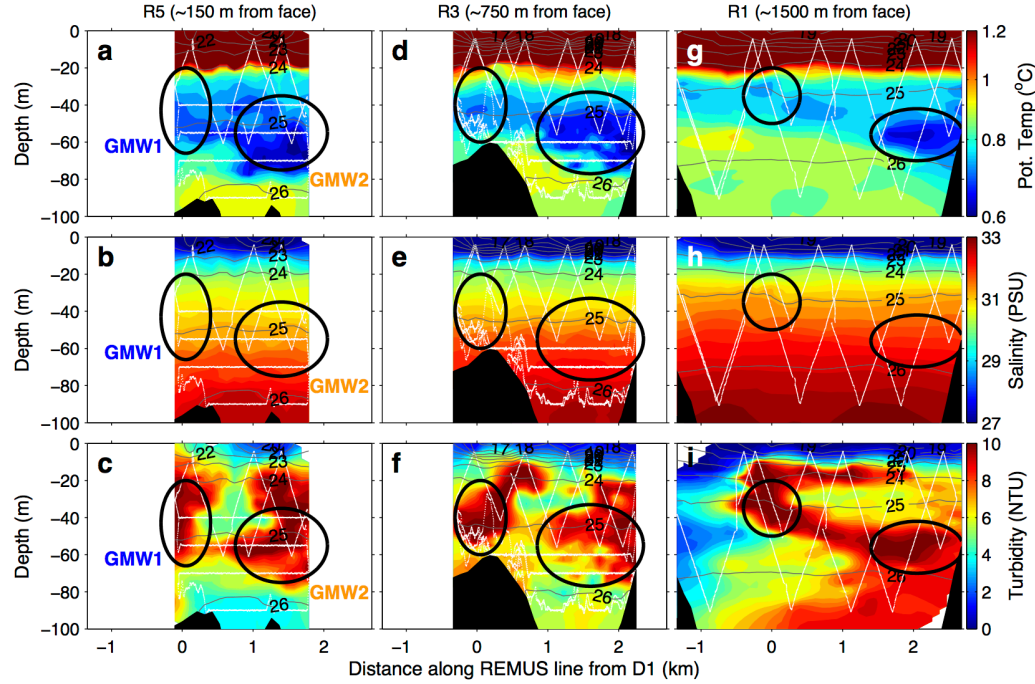
1019 **Fig. 1. The Sarqardleq Fjord/Sarqardliup sermia outlet glacier system in West Greenland.** Modified
 1020 from NunaGIS 1:100,000 map (Asiaq, Greenland Survey). Sill locations shown in red. Fig. 3 location
 1021 shown in red box.



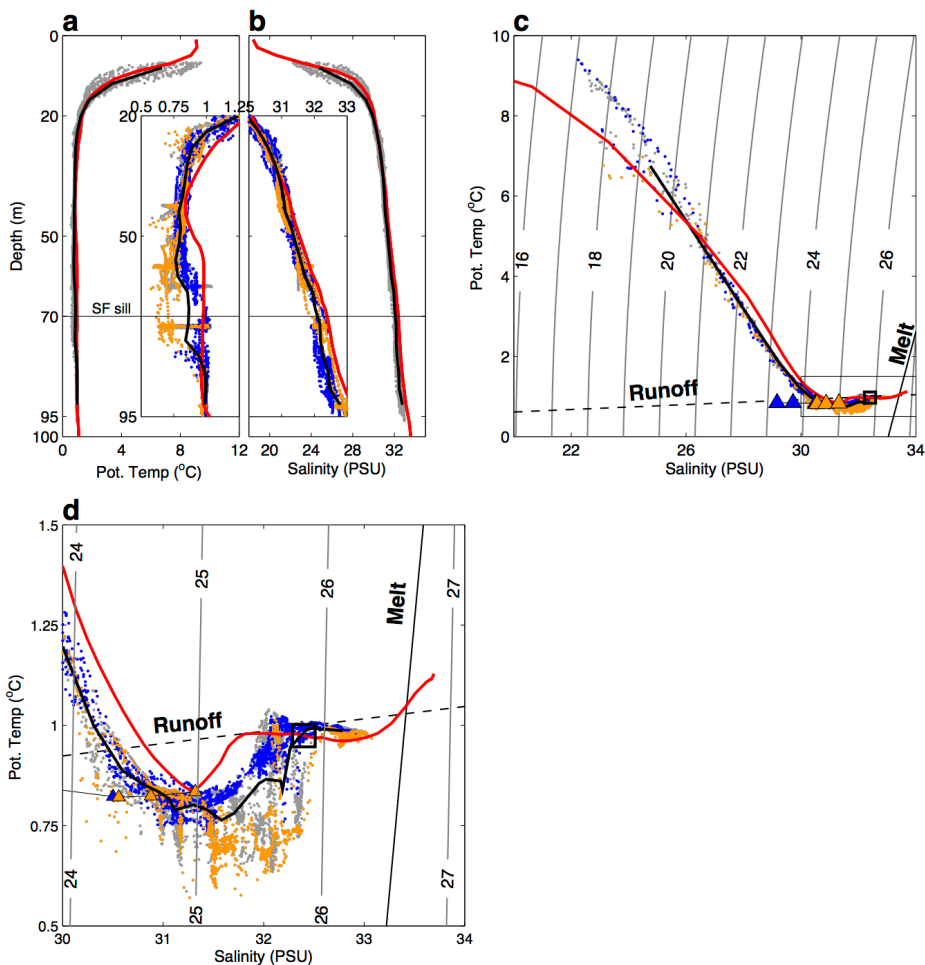
1025
1026 **Fig. 2. REMUS-100 AUV and past Sargardliup sermia terminus positions in Sargardleq Fjord. (a)**
1027 REMUS-100 AUV before deployment in Sargardleq Fjord. Note dense ice cover along Sargardliup
1028 sermia terminus. **(b)** Sargardliup sermia terminus 1975–2013 summertime positions digitized from the
1029 Landsat archive (<http://earthexplorer.usgs.gov/>) over fjord bathymetry and subglacial topography (see
Fig. 3). Front position dates are listed in the legend as year and day of year.



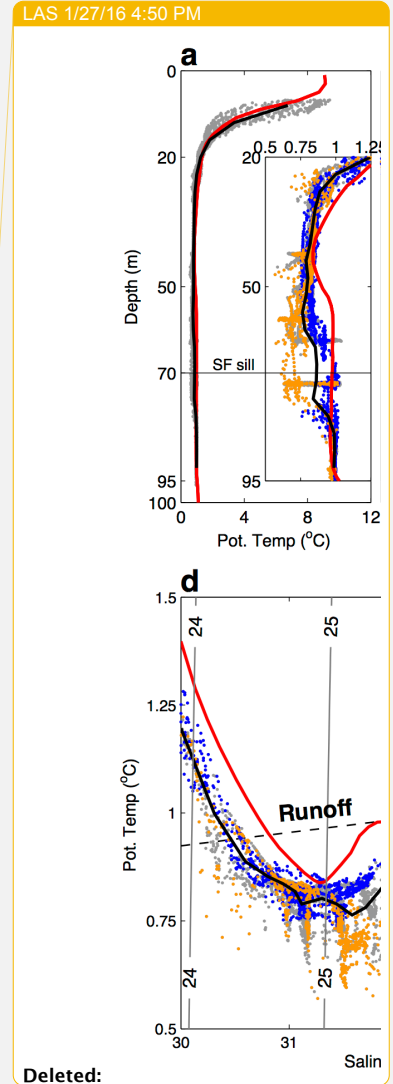
1030
1031 **Fig 3. July 2012 Survey of Sarqardleq Fjord.** Sarqardleq Fjord bathymetry (10-meter colored contours
1032 below sea level within fjord) and Morlighem et al. (2014) [bedrock elevation map](#) (10-meter colored
1033 contours above and below sea level outside of fjord) are shown. The Sarqardliup sermia front position and
1034 coastline from a June 19, 2012 Landsat image are mapped in red and black [lines](#), respectively. Depth
1035 measurements collected during July 2012 field operations used to create the Sarqardleq Fjord bathymetry
1036 are plotted as grey dots over the contoured bathymetry. REMUS transects R1–R5 are shown in black,
1037 with LBL transponders mapped with red triangles. Subglacial subcatchments C1, C2, and C3 dividing
1038 lines from MBM2014 analysis are mapped in dashed blue line, with the location of D1, D2, and D3
1039 subglacial discharge channels along the submerged terminus shown with thin black arrows. CTD casts are
1040 shown with diamonds: white diamonds are CTD casts along R1 used in REMUS cross-calibration, and
1041 the blue, gold, and grey diamonds are CTD casts 1, 2, and 3 that were taken along R5 within GMW1,
1042 GMW2, and the region between GMW1 and GMW2 (outlined in blue, gold, and white, respectively).
1043 Three proglacial stream entries to Sarqardleq Fjord are shown along the northeast and southwest fjord
1044 coastlines with thick black arrows.

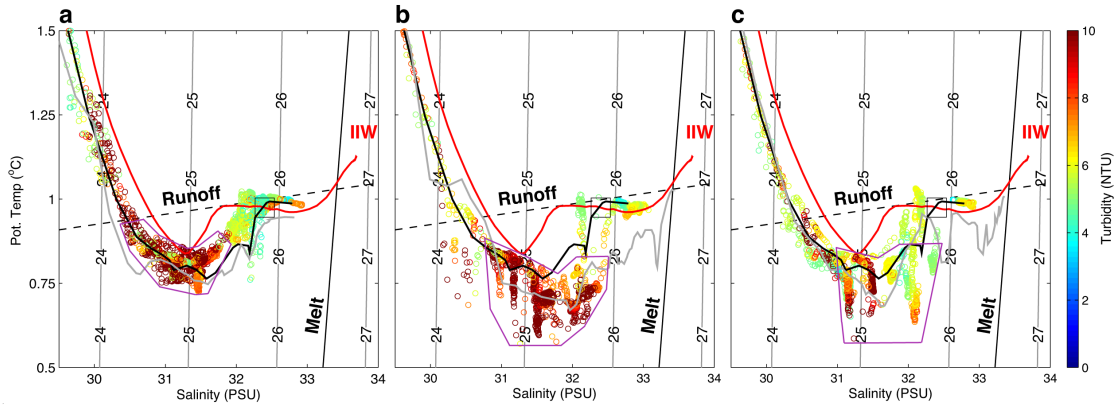


1045
1046 **Fig. 4. Select REMUS Across-Fjord Sections.** θ ($^{\circ}$ C), S (PSU), and turbidity (NTU) sections along
1047 REMUS lines (a–c) R5, (d–f) R3, and (g–i) R1 from 0 to 100 m depth. Sections are oriented looking
1048 away from the terminus, with the southwestern end of the section on the left. Across-fjord transect
1049 distance is plotted as horizontal distance along section, with 0 km located at the intersection of the
1050 REMUS section with an along-fjord line running from D1 to the southwestern LBL transponder along R1
1051 (Fig. 3). GMW1 and GMW2 regions identified by black ellipses, and labeled in blue and gold,
1052 respectively in a–c. Isopycnals plotted in grey, REMUS mission tracks shown in white (Table 1), and
1053 bathymetry shown in black (Fig. 3).

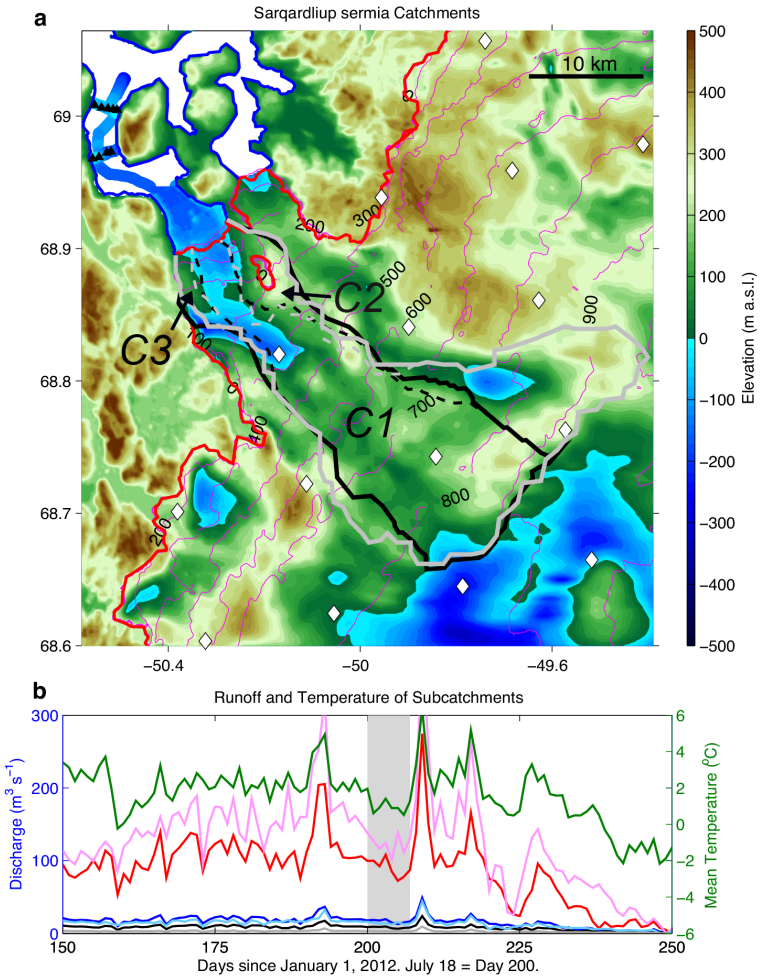


1054
1055 **Fig 5. Glacially Modified Water in Sarqardleq Fjord.** θ ($^{\circ}\text{C}$) (a) and S (b) profiles for R4 and R5
1056 measurements over the full water-column depth (grey), with the average of R4 and R5 measurements and
1057 the ambient fjord waters in black and red, respectively. Panel a and b insets show same data from 20–95-
1058 m depth over a finer θ or S range, with measurements taken within the GMW1 and GMW2 regions along
1059 R4 and R5 (Fig. 3) shown in blue and gold, respectively. θ /S plots of R4 and R5 measurements (c) (colors
1060 same as in a and b), with melt and runoff mixing lines. Intersection for melt and runoff mixing lines set to
1061 CTD2 properties at grounding line depth (Fig. 6 b). Black square along ambient fjord water profile shows
1062 θ /S properties at sill depth (70 m). θ /S results for the Jenkins (2011) plume modeling (Table 4) of D1
1063 (blue triangles) and D2 (gold triangles) shown. (d) Same data as in c over finer θ /S range indicated by
1064 thin black box in c.
1065





1068 **Fig. 6. Turbidity of Glacially Modified Waters.** θ ($^{\circ}$ C) and S (PSU) profiles from the regions along R4
1069 and R5 outlined in blue (GMW1 region) (a), gold (GMW2 region) (b), and white (the region between
1070 GMW1 and GMW2) (c) in Figure 3, with turbidity plotted as the color of the point. CTD1 (a), CTD2 (b),
1071 and CTD3 (c) are plotted in grey. The GMW region in θ /S space is outlined in purple. The average of all
1072 R4 and R5 measurements and the ambient fjord waters are plotted in black and red, respectively. Black
1073 square along ambient fjord water profile shows θ /S properties at sill depth (70-m).



1074
1075 **Fig. 7. Sarqardliup sermia catchments and discharge.** **a)** Estimated Sarqardliup sermia catchment
1076 (thick black line) and sub-catchments C1, C2, and C3 (dashed black line) from the MBM2014 analysis
1077 over Morlighem et al. (2014) bedrock elevation map (filled contours) and ice sheet surface (magenta
1078 contours). BBM2013 catchment and subcatchments outlines in thick solid and dashed grey lines,
1079 respectively. Ice sheet margin and coastlines shown in red and blue, respectively. RACMO2.3 11-km
1080 resolution grid points shown with white diamonds. Sarqardleq fjord bathymetry and outer Sarqardleq
1081 fjord CTD positions (black triangles) and depth measurements also shown. **b)** Daily C1, C2, and C3
1082 subcatchment MBM2014 RACMO2.3 discharge estimates (red, blue, and black lines, respectively) and
1083 daily average RACMO2.3 temperature (green line) across the Sarqardliup sermia subcatchment C1 for
1084 DOY 150–250, 2012. Daily C1, C2, and C3 subcatchment BBM2013 RACMO2.3 discharge estimates in
1085 pink, cyan, and grey lines, respectively. Dates of REMUS and CTD sampling from DOY 200–207
1086 marked by grey bar.

